BRNO UNIVERSITY OF TECHNOLOGY
VYSOKÉ UČENÍ TECHNICKÉ V BRNĚ

FACULTY OF MECHANICAL ENGINEERING
FAKULTA STROJNÍHO INŽENÝRSTVÍ

INSTITUTE OF PHYSICAL ENGINEERING
ÚSTAV FYZIKÁLNÍHO INŽENÝRSTVÍ

DETERMINATION OF DEVICE GEOMETRICAL MISALIGNMENTS INFLUENCE ON DIMENSIONAL MEASUREMENTS IN X–RAY MICROCOMPUTED TOMOGRAPHY

STANOVENÍ VLIVU NEPŘESNOSTÍ GEOMETRIE PŘÍSTROJE NA ROZMĚROVÁ MĚŘENÍ V RENTGENOVÉ POČÍTAČOVÉ MIKROTOMOGRAFII.

MASTER'S THESIS
DIPLOMOVÁ PRÁCE

AUTHOR **Bc. PAVEL BLAŽEK**
AUTOR PRÁCE

SUPERVISOR **Ing. TOMÁŠ ZIKMUND, Ph.D.**
VEDOUCÍ PRÁCE

BRNO 2020

BRNO UNIVERSITY OF TECHNOLOGY
FACULTY OF MECHANICAL ENGINEERING

Specification Master's Thesis

Department:	Institute of Physical Engineering
Student:	**Bc. Pavel Blažek**
Study programme:	Applied Sciences in Engineering
Study field:	Physical Engineering and Nanotechnology
Supervisor:	**Ing. Tomáš Zikmund, Ph.D.**
Academic year:	2019/20

Pursuant to Act no. 111/1998 concerning universities and the BUT study and examination rules, you have been assigned the following topic by the institute director Master's Thesis:

Determination of device geometrical misalignments influence on dimensional measurements in X–ray microcomputed tomography

Concise characteristic of the task:

X–ray computed tomography (CT) is a non–destructive technique for imaging of the 3D structure of objects. One of the benefits of this technology is the possibility of shape and dimensional measurement of industrial parts. The acquisition process is complex and is influenced by several factors, which contribute to errors in the dimensional measurement. This topic belongs to very current research in this field and helps to better understanding about the uncertainty sources of in the CT acquisition process. This work studies and determines the influence of factors related to mechanical part of the CT systems. More specifically, it focuses on influence of a detector and a rotation axis misalignment for dimensional measurement. Furthermore, it includes also new reference objects design according to international standards for CT system calibration.

Goals Master's Thesis:

1. To study X–ray computed tomography and its aspects important for application in metrology.
2. To analyse the effect of geometrical misalignments of detector and rotation axis on dimensional measurements.
3. To create new reference objects suitable for the evaluation of dimensional measurement errors and calibration of industrial CT systems.
4. Tp evaluate measurement errors on a specific CT device.

Recommended bibliography:

CARMIGNATO, S., W. DEWULF a R. LEACH. Industrial X-Ray Computed Tomography. Springer, 2018. ISBN 978-3-319-59573-3

KRUTH, J. P., M. BARTSCHER, S. CARMIGNATO, R. SCHMITT, L. DE CHIFFRE a A. WECKENMANN. Computed Tomography for Dimensional Metrology. CIRP Annals. 2011, roč. 60, č. 2, s. 821κ842. ISSN 0007-8506. Dostupné z: DOI:10.1016/j.cirp.2011.05.006.

FERRUCCI, M., LEACH, R.K., GIUSCA, C., CARMIGNATO, S. and DEWULF, W., 2015. Towards geometrical calibration of x-ray computed tomography systems—a review. Measurement Science and Technology, 26(9), p.092003.

Deadline for submission Master's Thesis is given by the Schedule of the Academic year 2019/20

In Brno,

L. S.

prof. RNDr. Tomáš Šikola, CSc.
Director of the Institute

doc. Ing. Jaroslav Katolický, Ph.D.
FME dean

Abstract

This thesis deals with geometrical misalignments of X-ray computed tomography (CT) device components. It focuses on their adverse effects on metrological CT measurements and on the methods which can be used to eliminate them. Results of simulations of CT measurements with misaligned detector and rotation stage are present, showing which misalignments plays the most significant role in the measurement. The practical part deals with HeliScan microCT, which implements a unique calibration algorithm to eliminate errors from misaligned CT geometry. New reference objects (plates with ruby spheres and calibrated zircon sphere) are developed for the CT system complying with the requirements of guideline VDI/VDE 2630 1.3. for metrological performance testing of CT devices. Testing objects suitable for a larger field of view were manufactured, calibrated, and successfully tested in CT measurement.

Abstrakt

Tato práce se zabývá geometrickými nepřesnostmi v geometrii rentgenového počítačového tomografu (CT přístroj). Především jejich vlivem na výsledky metrologických měření a metodami kterými lze tyto negativní efekty eliminovat. V práci jsou prezentovány výsledky simulací CT měření v softwaru aRTist při kterých byli nastavovány nepřesnosti v pozici detektoru a osy rotace vzorku. Ukazuje se tak, které geometrické faktory mají na měření největší vliv. Praktická část se pak zabývá CT přístrojem HeliScan, který využívá unikátní rekonstrukční algoritmus k eliminaci geometrických nepřesností. Jsou vyvinuty referenční objekty (pláty s rubínovými kuličkami a zirkonová koule), které splňují požadavky normy VDI/VDE 2630 1.3. na testování metrologických schopností přístroje. Objekty vhodné pro měření ve větším zorném polem byly vyrobeny, zkalibrovány a otestovány v CT měření.

Keywords

X-ray computed tomography, metrology, geometrical misalignments, calibration, calibration sample

Klíčová slova

rentgenová počítačová tomografie, metrologie, nepřesnosti geometrie, kalibrace, kalibrační vzorek

Reference

BLAŽEK, Pavel. *Determination of device geometrical misalignments influence on dimensional measurements in X–ray microcomputed tomography.* Brno, 2020. Master's thesis. Brno University of Technology, Faculty of Mechanical Engineering. Supervisor Ing. Tomáš Zikmund, Ph.D.

Determination of device geometrical misalignments influence on dimensional measurements in X–ray microcomputed tomography

Declaration

I hereby declare that this master thesis was written by me, under the supervision of ing. Tomáš Zikmund, PhD. Simulations in Chapter 6 were performed at the University of Padua under the supervison of prof. Simone Carmignato and in consultation with Elia Sbettega. Design of reference objects in Chapter 7 were consulted with Ing. Václav Duchoň and Bc. Vaclav Hortvík from Czech metrology institute Brno. I have listed all the sources of information used in this master thesis.

.....
Pavel Blažek
June 25, 2020

Acknowledgements

I want to thank my supervisor Tomáš Zikmund, for useful advice and guiding me during my entire work in the Laboratory of X-ray micro and nano computed tomography.

I would also like to thank Professor Simone Carmignato from the University of Padova and his Ph.D. student Elia Sbettega. They supervised and consulted my work on an interesting simulation study of geometrical misalignments during Erasmus traineeship in Padova.

I would also like to thank my family, which has supported me during the entire study, especially to my wife. If you were not taking care of me during the writing of this thesis, I would never have finished it.

Contents

Chapter 1

Introduction

X-ray computed tomography (CT) is an advanced imaging technique, widely used in industry for nondestructive analysis of inner and outer structures of objects. In the early 1970s, CT emerged as a tool for medical diagnosis. The technological development allowed later practical applications in the industry, for material analysis and nondestructive testing. With the improvement of measurement quality and accuracy, CT also entered the field of dimensional metrology. In the present, many producers of industrial CT systems have dedicated metrological systems in their portfolio and focus on improving the precision of the measurement to increase the impact in the field of dimensional metrology.

In CT measurement, an object is irradiated by an X-ray beam, and an X-ray detector acquires 2D projections from multiple directions (depending on the chosen measurement strategy). The 3D volume of the object is backwards reconstructed from the projections using mathematical algorithms [1] (detailed basic principles of CT are given in Chapter 2). Possibility to reconstruct the entire object and its inner features without the disassembly or destruction of the object is the main benefit of the CT over conventional tactile or optical coordinate measuring machines (CMM) [2]. Reconstructed volume can be easily visualized and used for various types of analyses even after a longer period of time, without the need to remeasure the object again. In contrast with tactile CMMs, CT does not need to apply force to object surface, which avoids errors from material deformation. CT measurement is limited by the tested object dimensions and density of its material due to the maximum penetration abilities of the X-ray beam.

Despite the great abilities of CT technology, the establishment of traceability and stating uncertainty of CT dimensional measurement is still a challenging task due to the presence of many factors that are often dependent on each other. Evaluation of these factors is topic of current research aiming to establishment CT as a reliable metrological tool. One of the critical factors is the geometry of the CT system. The deviation between actual geometry and geometry used in the 3D tomographic reconstruction from 2D projections leads to image artifacts and measurement errors [3, 4, 5]. Therefore, it is necessary to know the CT system's geometry and correct its negative effects to achieve high measurement accuracy. Several different methods of geometry calibration have been presented in literature [3, 6, 7, 8].

The problem of geometrical misalignments is one of the research topics in the Laboratory of X-ray micro and nano computed tomography on CEITEC BUT also due to the presence of the HeliScan micro CT device. It implements a unique reconstruction approach that can correct errors in CT system geometry using only the measured data itself, resulting in high-quality data without any additional reference scans. One of the demands of the HeliScan manufacturer is the evaluation of the HeliScan calibration approach in dimensional

measurements. Another opportunity to focus on this topic was given by collaboration with the University of Padova, which allowed us to take part in broader research of this topic and perform an extensive simulation study of geometrical misalignments and analyze their effect on dimensional measurements.

Chapter 2

Principles of X-ray computed tomography

This chapter will introduce the basic principles of CT and describe the main parts of lab-based CT devices, and it functions. The basic principle of CT can be described as follows. X-ray tube generates X-rays (Section 2.1), which penetrate the analyzed sample. Penetrating X-rays are attenuated due to absorption and scattering. Attenuation depends on the penetrated length and material composition and density (so on the coefficient of attenuation μ) and on the energy of the penetrating X-ray radiation. The detector collects attenuated and unattenuated X-rays and records radiographs of the sample. In the case of lab-based CT systems, detector and X-ray tube are usually stable while the sample is moving (rotating or performing other movements depending on used CT trajectory), so that radiographs are recorded from multiple positions. Acquired projections are reconstructed to obtain tomographic cross-sections (slices) from which the 3D volume is composed. Tomographic data can be used for further analysis, such as defects detection, determination of porosity, or dimensional measurements.

2.1 X-ray generation

X-rays are form of electromagnetic radiation with wavelength from 0.01 to 10 nm corresponding to frequency range 30 PHz to 30 EhZ and energies in the range 100 eV to 100 keV. In lab-based CT devices, energies above ten keV up to hundreds of keV are commonly used. X-rays can be generated by X-ray tubes, linear accelerators, or synchrotrons. Here, principles of X-ray generation will be explained on an X-ray tube with reflexive target, most common source used in lab-based industrial CTs. X-ray tube consists of electron source (cathode), target (anode) and electron optics, all enclosed in a vacuum chamber. Electrons are emitted from the cathode and focused on the target. Interaction between electrons and target atoms generates X-rays. Parameters of X-ray tube: applied voltage, electron current, spot size, target type, and material and filtering effect influences characteristics of X-ray beam [9].

The cathode is usually made of tungsten filament, which is heated by transmitting electric current (so-called Joule effect). As the kinetic energy of electrodes increases, they overcome the binding energy to the atoms and are emitted. This process is called thermionic emission. The anode consists of a metal target (most commonly tungsten or molybdenum) embedded on a heat conductor (usually copper). Source and target are connected to the

a voltage generator. Electrons are accelerated towards anode, creating a tube current and hitting the target due to electric potential difference. The energy of impacting electrons E_e depends on acceleration voltage V

$$E_e = eV, \tag{2.1}$$

where e is electric charge of electron. To achieve small spot size, the electron beam is focused on the target by electron optics. When electrons hitting the target are decelerated, over 99% of energy is convert to heat and less then 1% to X-rays. Three types of interactions leading to X-ray generation may occur: impacting electron deceleration by the target atom nucleus electric field, electron transition due to ejecting of a inner shell electron and collision of an impacting electron with a nucleus [10]. Their illustration and relationship to X-ray spectrum is shown in Figure 2.1.

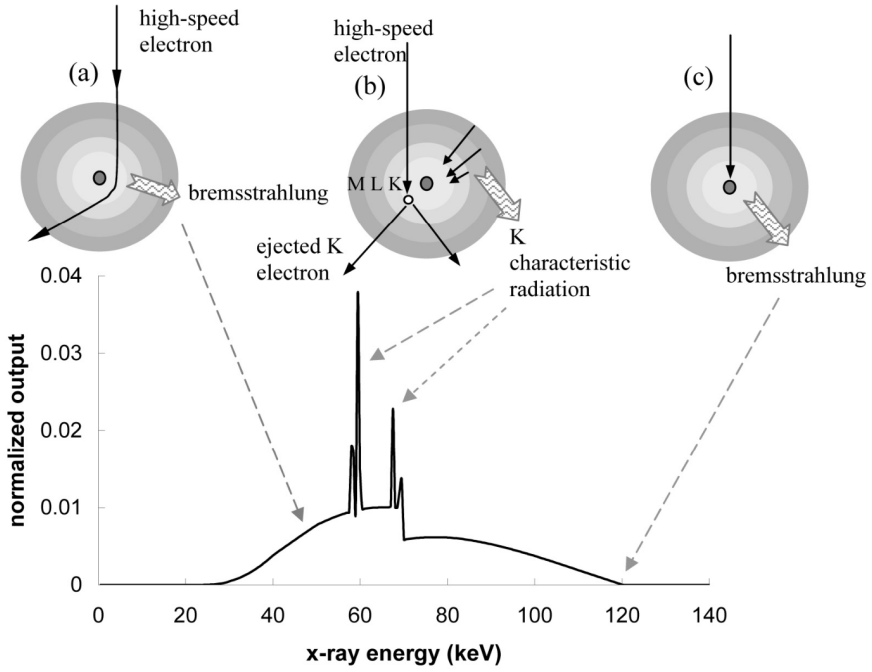

Figure 2.1: Example of the X-ray energy spectrum of an X-ray tube with tungsten target operating at 120 kV with additional filtering to remove low-energy X-rays. Illustration of electron interaction with a target and its relationship to the X-ray tube energy spectrum. (a) Bremsstrahlung radiation (b) Characteristic radiation (c) Interaction with nucleus. (Image from Hsieh 2015 [10]

X-ray spectrum consists of two types of radiation - *bremsstrahlung* and characteristics radiation. First type occurs when the fast electron approaches close to the nucleus and is deflected and decelerated due to Coulomb force (Figure 2.1 a). Lost energy during this interaction is emitted in form of X-ray radiation called *bremsstrahlung*. Energy of this radiation depends on kinetic energy loss during the interaction. Amount of emitted photons and their energy depends on the trajectory of electron and the proximity to atom nucleus. Its spectra is continuous. Highest energy photon (with energy corresponding to tube voltage) is emitted when all electron energy is lost. This happens when electron collides with atom nucleus (Figure 2.1 c)). The probability of this collision is very low, therefore intensity of X-rays with maximum energy is near zero. Total intensity I of bremsstrahlung

caused by a particle of mass m, charge Ne hittig target with atom number Z is proportional to [10]

$$I \approx \frac{Z^2 N^4 e^6}{m^2}. \tag{2.2}$$

This formula shows that bremsstrahlung radiation intensity increases with atomic number of target material. Low energy X-rays are often removed using filter on the tube.

Characteristic radiation cause high-intensity peaks in X-ray spectra (Figure 2.1 b)). Impacting electron can interact with inner shell electron (called K, L, M ...) of target atom while removing it from its orbital. Electron from outer shell, most frequently from the nearest shell, fills the vacant place. This process generates X-ray photon of energy equal to energetic difference of the shells, hence depends on the anode material.

2.2 Interaction of X-rays with matter

X-rays generated in the X-ray tube are attenuated in measured sample. Attenuation is caused by four main processes: the photoelectric effect, Compton scattering, Rayleigh scattering and electron-positron pair production [11, 4]

Photoelectric effect

When the X-ray photon has higher energy than binding energy of electrons in atom, it can be absorbed ejecting the *photoelectron* from the atom. Energetic balance of this interaction can by described by

$$E_\mathrm{p} = E_\mathrm{b} + E_\mathrm{pe}. \tag{2.3}$$

Electron binding energy E_b and energy of the *photoelectron* E_pe is equal to sum of energy of the incident photon E_p. Vacant space is then filled with electrons form higher orbitals while emitting Auger electrons or X-ray photon of the energy equal to energetic difference between the shells. Absorption is proportional to atomic number Z of the material and energy of the incident photon (with wavelength λ). Absorption coefficient caused by photoelectric effect can be estimated as [12]

$$\mu_\mathrm{pe} \propto Z^4 \lambda^3. \tag{2.4}$$

Materials with high atomic number (such as lead) have strong absorption of X-rays and are often used for shielding of the radiation [4]

Compton scattering

Compton scattering (also called inelastic scattering) occurs when a photon has higher energy than the binding energy of an electron (usually in outer, mainly in valence shells). The incident X-ray photon interacts with the electron transferring only part of energy and kicking it out of the atomic shell. As an implication of the law of energy and momentum, conservation photon is scattered in different direction with lower energy and higher wavelength. Energy transfer can be described by

$$E_\mathrm{p} = E_\mathrm{e} + E'_\mathrm{p}, \tag{2.5}$$

where E_p and $E'_\mathrm{p}$is kinetic energy of the incident and scattered photon respectively and E_e is energy of the ejected photon [13]. Probability of Compton scattering does not depend

on the material atomic number, but on the electron density. The coefficient of attenuation caused by Compton scattering is defined as [12]

$$\mu_{\text{compt}} = n\sigma_{\text{Compton}}, \tag{2.6}$$

where n is electron density and σ_{Compton} is total cross-section for Compton scattering [14, p. 155].

Rayleigh scattering

The electric field of incident photons carries energy that interacts with all electrons in an atom causing their oscillation. The atom is excited and immediately emits a new photon of the same energy but in different direction. During the process of inelastic scattering, electrons are not ejected, and ionization does not occur [13]. The scattering angle of the photon increases with photon energy. This type of interaction has a low probability of occurrence in energy range used in industrial CT; it is important only for low energies [4].

Pair production

This effect occurs only for high energies of X-rays (mega-electron-volts). X-ray photon interacts with electric field of the atomic nucleus creating positron-electron pair. Newly created particles mutually annihilate emitting two photons in opposite directions [12].

2.2.1 Total attenuation

All these effects described above contribute to total attenuation. The total attenuation coefficient is defined as

$$\mu = \mu_{\text{pe}} + \mu_{\text{compt}} + \mu_{\text{ray}} + \mu_{\text{pair}}, \tag{2.7}$$

where μ_{ray} is the attenuation coefficient due to Rayleigh scattering, and μ_{pair} is the attenuation coefficient due to pair production. Contribution of particular effects depends on energy of the X-rays and irradiated material properties, as is shown in three examples of materials in Figure 2.2: carbon ($Z = 6$), aluminum ($Z = 13$) and tungsten ($Z = 74$). Compton scattering is dominant for higher energies and low atomic number materials (above 25 keV in case of carbon and 50 keV in case of aluminum). The photoelectric effect is dominant for lower energies. It is dominant in larger energy range in case of high atomic number materials (as tungsten), where furthermore, the characteristic absorption edges are noticeable.

Beer-Lambert law

X-rays are suffering exponential attenuation when traveling through the material. Assuming that the incident beam is monochromatic and the irradiated object's material is homogeneous, we can describe attenuation by a first-order differential equation

$$\frac{\mathrm{d}I}{I(x)} = -\mu \mathrm{d}x, \tag{2.8}$$

where I is intensity of X-ray radiation, μ is linear coefficient of attenuation and x is penetrated length. Integrating both sides and applying initial condition $I(0) = I_0$ we can obtain solution

$$I = I_0 \exp(-\mu x), \tag{2.9}$$

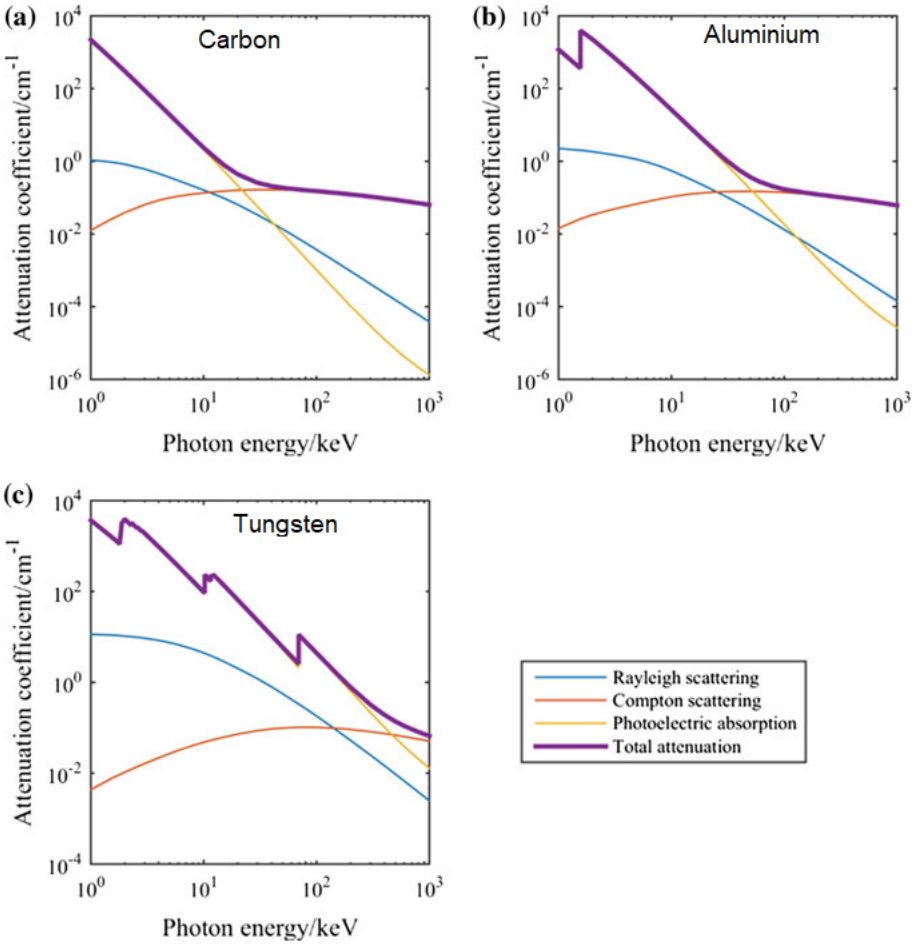

Figure 2.2: Attenuation coefficient for different materials (a) carbon, (b) aluminum (c) tungsten in relation to photon energy. Contribution of Rayleigh scattering, Compton scattering and photoelectric effect is shown. (Image from Carmignato 2018 [4]).

which is Beer-Lambert law [12]. Coefficient μ is generally not homogeneous through an object.For X-ray traveling along line Ψ is attenuation coefficient given by line integral

$$\mu = \int_{\Psi} m_a \mathrm{d}\Psi, \tag{2.10}$$

where m_a is material absorbance per length unit of ray trajectory [15]. As was already explained, attenuation coefficient depends also on X-ray radiation energy. Transmitted intensity of monochromatic X-ray beam after penetration of length L can be described as

$$I = I_0 \exp\left(-\int_0^L \mu(x)\mathrm{d}x\right), \tag{2.11}$$

and for polychromatic beam as

$$I = \int_0^{E_\mathrm{max}} I_0(E) \exp\left(-\int_0^L \mu(E,x)\mathrm{d}x\right). \tag{2.12}$$

Difference between monochromatic and polychromatic formula is origin of so called beam hardening artifact [12].

2.3 Detector

After the X-rays are attenuated in a measured object, they are captured by an X-ray detector, creating the projection images, which are then used as an input for 3D reconstruction of the measured object. The most often used types of detectors in industrial lab-based CT devices are scintillation detectors with a flat panel. High-resolution CTs with a smaller field of view (nanoCT devices, synchrotrons) use light senors based on CCD or CMOS architecture [15].

Scintillation detectors consist of scintillation crystal and a photon detector. X-ray photons are hitting the scintillator, exciting its atoms. During the deexcitation process, photons of visible light wavelength are emitted and consequently directed to light sensors (such as a photo-multiplier tube).

Flat-panel detectors typically consist of a grid of elements composed of a photodiode and a thin-film transistor on a substrate. Pixel matrix is coated with scintillation material, usually cesium iodide (CsI). Finally, the cover layer is used for protection from mechanical damage.

The most important characteristics describing the detector's quality are detection efficiency, stability over time, energy resolution, afterglow, response time, and dynamic range [16].

Digital images are acquired from the detector as a 2D matrix of gray values. Gray values are representing the amount of X-ray attenuation in the sample (ratio between initial intensity and intensity after transmission $\frac{I_0}{I}$). Detector acquires projections with set exposure time.

2.4 Kinematic system

The CT principle is based on the acquisition of X-ray projections of the sample from multiple directions, by rotating or linear shift of the sample. Kinematic must provide that projections

are acquired precisely in positions which will be subsequently used in the geometry of the reconstruction. In case of a circular scan, the projection is always acquired after turning the sample by angular step α_i.

In lab-based CT systems, the acquisition is usually performed by rotating the sample on a table while X-ray tube and detector are stable. The kinematic system must provide high precision movement and stability of the components. It enables movement in several degrees of freedom:

- sample rotation (α) - rotating table provides rotation of the sample to obtain projections,
- horizontal axis z - allows changes of magnification by the movement of the sample or detector,
- horizontal axis x - provides table movement along detector to set proper position or detector shift for extending the field of view ,
- vertical axis y - provides movement of the sample or the tube and the detector, necessary for scanning with helical trajectory.

Many possible trajectories can be used to obtain images - most common is circular and helical trajectory, but also others are possible (laminography or free trajectories).

2.5 Reconstruction

After the acquisition of projections is finished, the reconstruction is performed by means of mathematical algorithms to obtain 3D volume of the measured sample.

As was already explained, X-rays are suffering exponential loss passing through an object which can be described by Lambert-Beer law (eq. 2.11) (we assume monochromatic beam and for simplification only 2D object, so reconstruction of only one tomographic slice). Total attenuation of X-ray after object penetration can be then described as

$$\ln\left(\frac{I_0}{I}\right) = \int_{\Psi} \mu(\Psi)\mathrm{d}\Psi \equiv p_{\mathrm{s}}\Psi. \tag{2.13}$$

Function $p_{\mathrm{s}}\Psi$ represents distribution of material absorbance and depends on trajectory Ψ of the beam and on attenuation of material $\mu(\Psi)$) along the trajectory. Finding this function (assigning the correct attenuation value μ to each voxel) is central problem of tomographic reconstruction. CT device measures just the ration $\frac{I_0}{I}$ from several different position, so for different lines Ψ [1].

Tomographic reconstruction is a very extensive topic. There is a variety of algorithms that can be divided into two categories: analytical and iterative [17]. The analytical approach solves the reconstruction problem in the form of a continuous differential equation modeling the objects as a mathematical function. Most commonly used is an algorithm called Filtered backprojection (FBP). Iterative methods formulate the reconstruction as an optimization problem. 3D volume is reconstructed and compared to real projections. Reconstruction parameters are iteratively adjusted until convergence of the results. Iterative reconstruction can provide better quality CT data. However, the high computation times prevent it from more extensive usage in industrial practice [1, 4].

2.6 Analyses on volumetric data

The reconstructed 3D volume consists of voxels, which are a volumetric representation of pixels. Each voxel is assigned a gray value, which ideally corresponds to the attenuation of the measured object material.

The reconstructed object can be imaged as cross-sections or by various methods in 3D. In case of further analysis, reconstruction is usually followed by surface determination or segmentation, which should determine interfaces between materials in the sample. There is a variety of methods which can be used - thresholding, searching form maximum derivative, etc. Surface determination is crucial for accurate results of subsequent analysis. Errors are often caused by image artifacts (beam hardening, metal artifacts, etc.) [18].

Various analyses can be performed on CT data - porosity detection and evaluation, wall thickness analysis, nominal-actual comparison, or dimensional measurements. Analyses can be performed accurately only when performed on high-quality data. It is, therefore, necessary to reduce the effect of various error sources as much as possible.

Chapter 3

Instrument geometry as an influence factor

CT measurement is influenced by many factors that are often dependent on each other. Study of these factors is a topic of current research aiming towards higher quality CT data and traceability establishment of CT dimensional measurements. Influence factors can be categorized into five groups [19]: factors connected with CT system hardware (X-ray source, detector, geometry), software data processing (reconstruction, data corrections, surface determination, and subsequent analysis), measured sample (its material and shape), environment (cabinet temperature, vibrations) and factors influenced by a CT operator (measurement parameters, fixture of the sample), see Figure 3.1. All importation influence factors are described in German guideline [20] or by other authors, for example [4, 18].

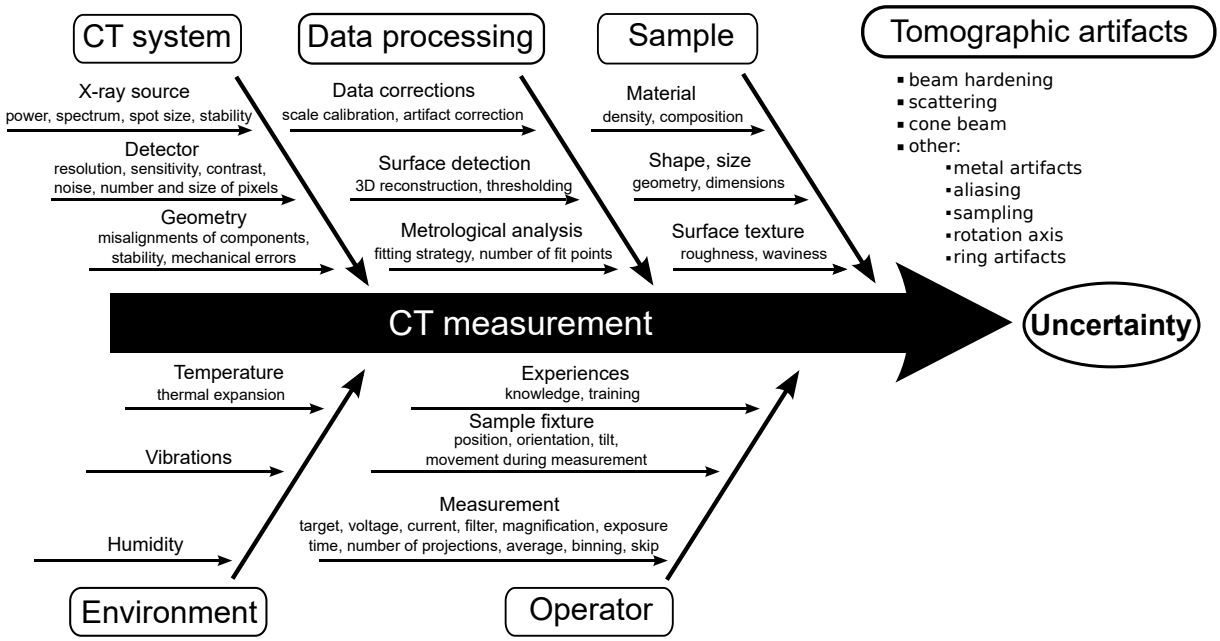

Figure 3.1: Overview of factors influencing CT measurement. According to [21]

One of the critical influence factors is represented by the presence of possible geometrical misalignments on the CT system components. The deviation between actual geometry and geometry used in reconstruction leads to image artifacts and measurement errors. This

chapter will summarize known effects of geometrical misalignments on measurement according to existing literature and introduce methods eliminating these effects. Overview of research that contributed to the development of geometrical calibration procedures presents Ferrucci et al. in [3]. Authors summarize geometrical influence factors and methods of their determination and describe their effect on reconstructed data, particularly dimensional measurements. Overview of error sources associated with the positioning system is also given in [4].

3.1 Cone-beam CT geometry model

The relative position of the X-ray source, rotation stage, and detector define the CT system geometry. A coordinate system is defined to describe aligned system geometry. It is depicted in Figure 3.2. It corresponds to the coordinate system of simulation software aRTist used in chapter 6. The magnification axis z is given by line from the X-ray source's central point to the detector. y-axis is parallel to the rotation axis. x-axis is then orthogonal to y- and z axis forming Cartesian coordinate system [3]

CT system is considered aligned when it sat satisfies these conditions (from [3]):

1. The intersection of the magnification axis with the detector is coincident with the center of the detector,
2. the magnification axis is normal to the detector,
3. the magnification axis intersects the rotation axis of rotation at a 90° angle and
4. rotation axis is parallel to columns of detector matrix.

Distances between detector center and source (SDD) and distance between the intersection of rotation axis with magnification axis and source (SRD) are assumed to be accurately known.

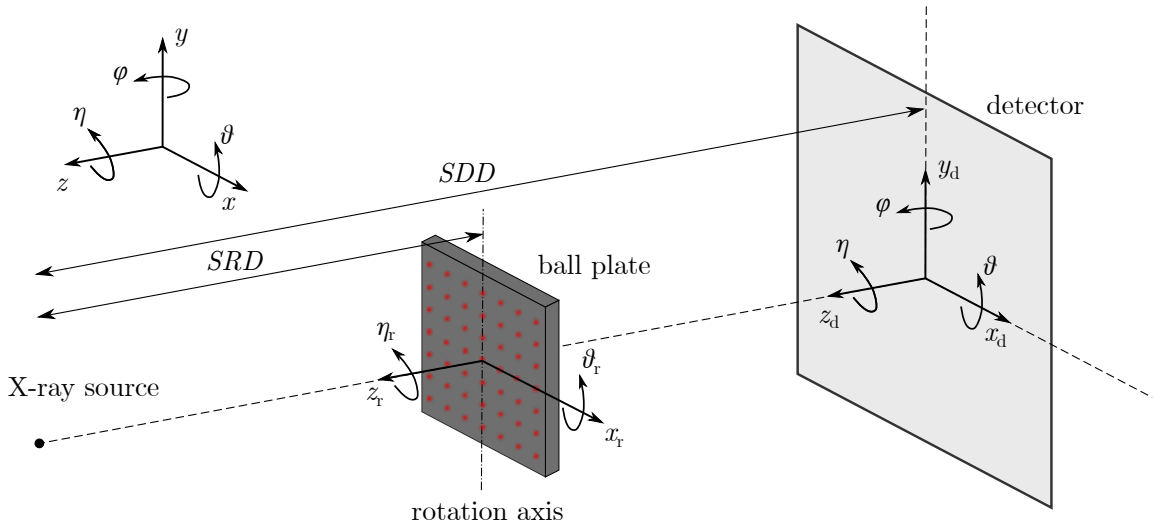

Figure 3.2: Coordinate system used for description of CT system and misalignments of its components

Deviation from the condition 1 is detector shift and can be described by position of the detector center (x_d, y_d). Deviations from condition 2 are detector out-of-plane rotations - slant φ around y-axis and tilt ϑ around x-axis. Deviation from the condition 3 is rotation axis tilt ϑ_r, deviation from condition 4 is detector out of plane rotation (skew) η_d or rotation axis skew η_r. Inaccurate knowledge of distances SDD and SRD leads to detector and rotation axis shift in magnification axis: z_d and z_r respectively. These errors and their effect on CT measurement are summarized in Table 3.1. Detailed examination of these misalignments is a topic of simulation study in Chapter 6.

Also, other errors associated with CT geometry can appear. The detector is assumed to be perfectly planar and its pixels to be uniform. The inaccuracy of angular index (rotation step) leads to reconstruction errors. Misalignments of geometry are also caused by errors in the mechanical motion of the kinematic axes (positioning of the rotational stage or detector) as straightness and squareness errors [3]. Geometrical errors may change through the measurement time due to the instability of the system.

3.2 Effect of geometrical misalignments on CT dimensional measurements

Assessment of CT dimensional measurement errors is usually performed by comparing dimensional measurements of an object's CT data with its reference measurement, utilizing tactile or optical CMM. These errors are result of various error sources, including uncertainty of reference measurement. Unidirectional measurements should be used to access errors connected with CT geometry and eliminate other error sources. It is useful to use objects made of spheres, spherical caps or circular holes. Unidirectional characteristic of the distance between centers of spheres or circular holes allows to reduce the effect of surface determination on the result and focus on the errors connected with image scale. Most of the so far published studies utilize simulations of CT measurement, avoiding potentially expensive intervention to real CT hardware. Benefit of simulation is that system geometry, and reference object can be exactly determined, and other error sources that could appear in real CT measurement can be avoided. On the other side, the differences between simulation and CT measurement must be taken into account when interpreting the results.

Several simulation studies were performed focusing on the effect of geometrical misalignments on dimensional measurements. Wenig et al. [22] performed a simulation-based investigation of selected influence factors on CT dimensional measurement. They evaluated errors of inner diameters and inner and outer linear measurements on alloy object. Besides other influence factors, they tested detector and rotation axis misalignments. Detector tilt by 1° had the most critical effect. Further analysis performed on a ball bar phantom showed that tilt of detector corresponding to 1/4 pixel and less has a negligible effect on measurements. The second strongest influence had shift of rotation (rot.) axis by 700 µm. The noticeable influence had also rot. axis tilt by 1°. Shift by 350 µm, which corresponds to 1-pixel shift and detector slant and skew by 1° had negligible effects.

Most authors used simple objects such as ball bars or ball plates for analysis. Authors of [23] developed a simulation model with a simplified phantom consisting of two balls to observe the effect of different geometrical errors. Results indicated that errors in source and rotation axis position had more significant effect on measurement error than detector position error. Measurements performed with high magnification were more sensitive to positioning errors than low magnification measurements. They found that detector tilt

has high impact on vertical distances and detector slant on horizontal - both have similar magnitudes.

Ferrucci et al. [24] presented a simulation study of detector angular misalignments. They focused on higher angular values - for detector tilt (rotation around x-axis) and slant (rotation around y-axis) 5° and 10° and for skew (rotation around z-axis) 1° and 2°. They evaluated the effect of these misalignments by checking the centroid position and the form errors of spheres at the cylindrical phantom. Their investigation showed that sphere centroids deviations are different in the top and bottom part of the volume due to detector tilt. For detector slant, horizontal deviations point outwards from rot. axis and vertical deviations point towards mid-plane. The magnitude of deviations increases with the distance of the sphere from rot. axis. Detector skew does not have a significant impact on centroid position (compared to slant or tilt). Instead, it causes artifacts of spheres. The sphere is reconstructed as two overlapping spherical objects, each individually having a lower material attenuation value than the overlapping section. Similar artifacts also appear due to detector slant. Ferrucci [25] also performed a study of multiple detector rotations and rotation stage errors effect.

In [26], an experimental study on detector tilt with ball bar positioned parallel to rot. axis was performed. It showed that the tilt of detector causes large errors in the vertical direction, which are symmetrical about the x-axis. Highest errors appeared for length 15 mm (28 µm for $\vartheta = 1.5°$), for larger and smaller lengths, maximum error decreases, for 30 mm length, error is around zero. Similar differences also appeared for the diameters of spheres. It was shown that distance error depends on the position of measured length in the measurement volume.

Ametova et al. [27] proposed a geometrical error model of uncertainty determination based on the forward- and back-projection of an object's surface points, which is much less time-consuming than Monte Carlo simulation methods. The model was able to capture errors of object edges and also estimate errors of dimensional measurements of sphere centers. Test on detector angular and linear misalignments confirmed that effects are not uniform through the measured volume, which corresponds to previous studies.

3.3 Correction of geometrical errors

Misalignments of system geometry have disturbing effects on the CT measurement. To avoid these effects geometry must be determined, followed by hardware alignment or adjustment of the reconstruction geometry accordingly. Several types of methods can be used to determine the system geometry. First category uses a reference object which is imaged and the geometry is deduced from projections or from 3D reconstructed data. In general, imaging methods apply principles of projection geometry. Coordinates of the reference object features in projection image depends on the geometry of the imaging system. Therefore, geometry of the system can be inversely determined from projection images. The summary of these methods is given in [25]. Usually an objects with spherical or circular markers which represent coordinate points are used. Objects are imaged in several rotation positions and this data is compared to the reference geometry and set of geometrical parameters is solved. There are also methods which do not need any special reference object but can perform the analysis on the data from the actual sample itself, they are called "online methods". Second category uses reference instruments such as laser interferometers to measure kinematic parameters of the system [3]. Here we will describe in more detail methods of scale calibration and online calibration methods which are used in Chapter 7.

Table 3.1: Overwiev of geometrical misalignments analyzed in this study. Short description of their effect. According to [3].

Parameter	Effect
z_r (shift of source to rotation axis distance) z_d (shift of source to detector distance)	An error in source to detector and source to rotation axis distance results in a scaling error of the measurement volume. Errors in magnification can be caused by drift of x-ray source and therefore can vary through scan [28].
x_d (detector shift in x-direction) y_d (detector shift in y-direction)	Deviations in the principal point from the detector centre can result in reconstruction errors (errors of form, double edges [27]) unless the reconstruction software can accommodate such deviations.
x_r (rotation axis shift in x-direction) η (detector skew, in-plane) η_r (rotation axis skew)	A horizontal shift of the rotation axis can result in reconstruction errors unless the reconstruction software can accommodate a non-central rotation axis. Similar effect have also detector skew and rotation axis skew.
ϑ_r (rotation axis tilt about x-axis)	A tilt of the rotation axis about the x-axis result in the object being magnified differently along the rotation axis.
ϑ (detector tilt, out-of-plane rotation) φ (detector slant, out-of-plane rotation)	Detector tilt and slant result in form errors due to changes in aspect ratio of similar objects at different regions of the detector. Errors in distances measurement are caused by magnification change in different parts of measured volume [3, 29].

3.3.1 Scale calibration

Scale identification is very important step to achieve precise and traceable dimensional metrology. In CT data it means identification of voxel size. Voxel size can be calculated from SDD, SRD and pixel size p as

$$vx = \frac{SRD}{SDD}\, p. \tag{3.1}$$

Distance between two points in CT volume is then calculated as $L = n \cdot vx$, where n is number of voxels between those points. n does not have to be integers as intra-voxel interpolation is often used in surface determination. Geometrical parameters of CT are subject of a number of error sources like thermal expansion, focal spot drift, vibrations or error in kinematic system and in distance encoders. It is, therefore, necessary to perform calibration.

If we assume accurate knowledge of p, distance error caused by bad determination of SDD and SRD can be described as

$$E = L_{\mathrm{ref}} - L = L_{\mathrm{ref}} \left[1 - \frac{SDD(SRD + z_{\mathrm{r}})}{SRD(SDD + z_{\mathrm{d}})} \right]. \tag{3.2}$$

Widely accepted and commonly used method of scale calibration is using reference objects, often ball bar or ball plate with calibrated distances L_{ref} between spheres to correct errors in image scale. The object is scanned prior, together or after the measurement of the actual sample. Voxel size is subsequently corrected according to original measured distance L_{CT} as [30]

$$vx_{\mathrm{corr}} = vx_{\mathrm{orig}} \frac{L_{\mathrm{CT}}}{L_{\mathrm{ref}}}, \tag{3.3}$$

where vx_{orig} is original value of voxel size used in calibration measurement.

More complex method of scale calibration can be performed by measuring the reference object in several position with different magnification. If we know the detector pixel size p and shift between the object position, we can determine distances SDD and SRD. Principle of this approach is derived in [31].

3.3.2 Online methods

Kingston et al. [8] proposed a method for compensation of geometrical misalignments which uses acquired data itself, without usage of any other calibration artifacts. Fast reconstruction is performed on several slices with varying geometrical parameters (detector and rotation axis linear and angular misalignments) until sharpest reconstruction is found. These parameters are used to remapping acquired projection data to virtually aligned projections followed by standard reconstruction algorithm.

This auto-focus algorithm is implemented in reconstruction software of HeliScan micro CT system which is used in practical part of this work (Section 7.1). This method was developed aiming mainly to improve the image qualilty, its performance on improving dimensional errors is subject of testing in Chapter 7.

Chapter 4

Evaluation of metrological performance of CT systems

When the errors caused by influence factors described in previous sections are minimized, CT measurements can achieve high accuracy. CT can be then used not only for non-destructive analysis but as well in metrology. CT can be considered as coordinate measuring machine and similar characteristics of metrological performance as for testing conventional CMMs can be used. International standard series ISO 10360 describes methodology of verification and acceptance testing for many types of coordinate measurement systems. Part of ISO 10360 for CT systems testing is currently in development, first drafts have been already published for discussion in scientific and industrial community. At present, only a German national guideline VDI/VDE 2630-1.3 is available in this topic for the field of CT.

Aim of acceptance testing is to check whether the CT device meets the specifications stated by the manufacturer. Reverification tests are used to ensure the performance during the operation of the system. Both tests should be performed regularly and should reflect conditions of common usage of the system. All dominant errors sources should be taken into account. Manufacture should provide conditions under which the test should be operated. Result of the test should describe three-dimensional error behavior of the overall system. Two complementary test: local probing error test (P-test) and global length measurement error test (E-test) are used according to the ISO and VDI/VDE guidelines. These characteristics are compared to manufacturer's stated maximum permissible error values (MPE) to check the system performance [32, 4].

4.1 Probing error

P-test describes three-dimensional error behavior of the overall system within a very small measurement volume. Two characteristics are used: probing error of form (P_{F}) and probing error of size (P_{S}). For this test are usually used spheres or spherical caps made of suitable material with calibrated diameter and negligibly small error of form and roughness. CT data of the sphere measurement are analyzed by Gaussian fitting of the sphere on the surface. Probing error of form P_{F} is defined as "the span of the radial deviations of the measurement points from the calculated regression sphere" [32]. It can be calculated as

$$P_{\mathrm{F}} = R_{\max} - R_{\min}, \tag{4.1}$$

where $R_{\max}$ and $R_{\min}$ are the maximum and minimum distances from the center of the regression sphere to the probing points. The probing error of size P_{Size} is defined as the difference between measured diameter of the sphere D_{a} and reference diameter D_{r} and is calculated as [32]

$$P_{\text{S}} = D_{\text{a}} - D_{\text{r}}. \tag{4.2}$$

Probing error characteristics should be measured in multiple positions over the entire measurement volume (6 positions are recommended) for at least two magnifications. Diameter of the sphere used for evaluation shall be about 10 to 20% of measurement space diagonal [32].

4.2 Length measurement error

The global length measurement error test (E-test) describes behavior of the system within the entire measurement volume, corresponding characteristic is length measurement error (E). Length measurement error should be tested by measuring bidirectional length, which is defined as "distances between two points on different faces, assessed in opposite probing direction" [4], so that all important error sources are included. For this test gauge blocks or step gauges can be used. Length measurement error is then calculated as

$$E = L_{\text{a}} - L_{\text{r}}, \tag{4.3}$$

where L_{a} is measured length value and L_{r} is the calibrated length. Other option is to do the test on unidirectional length, for example distance between two sphere centers on ball plate or ball bar. Sphere distance error S_{D} is defined as difference between displayed value of test length (distance between centers of two balls) L_{ka} and calibrated length L_{kr},

$$S_{\text{D}} = L_{\text{ka}} - L_{\text{kr}}. \tag{4.4}$$

To include probing errors to the S_{D}, VDI/VDE guideline suggest two options. Method A suggests to add probing errors with correct sign to the sphere distance errors and determine length measurement errors E. Calculation can be then described by formula

$$E = S_{\text{D}} + P_{\text{S}} + \text{sgn}(S_{\text{D}} + P_{\text{S}}) \cdot P_{\text{F}}. \tag{4.5}$$

Second method B is more precise and suggests to make and additional bidirectional measurement of a short calibrated length (e.g. a gauge block or a two-point distance at a sphere). Length error E_{E} of this measurement can then be added to the error S_{D} as

$$E = S_{\text{D}} + E_{\text{E}}. \tag{4.6}$$

Chapter 5

Motivation and goals of the practical part

Result of previous researches shows that system geometry is an important influence factor of CT measurement and that misalignments of the CT systems components are one of the critical error sources. They can significantly decrease the quality of the CT data and cause errors in dimensional measurement. However, authors of previous studies used simplified models [23] and phantoms [22, 29] or study higher amplitude of misalignments [3], so their results must be interpreted carefully if applied to real CT measurement. Currently exist a variety of methods that can reduce these inappropriate effects either by proper hardware alignments and by using interferometers to measure the position of CT component or by determination of the system geometry and subsequent correction of the reconstruction algorithm. These methods are often expensive due to sophisticated hardware like laser interferometers [33] or time consuming due to the necessity to perform additional reference scans [3]. If these methods are used in metrological practice, it is crucial to know how well they perform in the reduction of measurement errors.

One of the CT devices located at CEITEC VUT HeliScan is equipped with reconstruction software, which can determine system geometry from the measurement data itself and adjust the reconstruction accordingly. It is able to avoid most critical error sources such as detector tilt and skew and magnification errors. The benefit of this approach is, that any additional scans of reference object or precise alignment of the system are not required. This approach was proven to increase the quality of the CT data [8], however, the performance in metrological measurements was not validated yet.

This thesis aims to improve the general understating of CT system geometry's influence on CT measurement and evaluation of methods which can be used to reduce these disturbing effects.

The first goal of this thesis is to perform an overview study of all important geometrical misalignments of CT components which can appear in practice of CT metrological usage and evaluate their effect on dimensional measurements. This study's results should clearly show which misalignments cause highest errors in CT dimensional measurements and should therefore primarily focus on hardware alignment and geometry calibration methods. The study will be performed on angular and linear shift of detector and rotation stage, including the effect of different magnifications. As an appropriate instrument, we will use software aRTist allowing simulations of CT scans with accurately determined geometry. We will also emphasise spatial and directional effect of misalignments in measured volume.

The second goal is to design new reference objects suitable for testing of metrological performance of this HeliScan microCT with a focus on its unique reconstruction algorithm. The objects should comply with the requirements of German guideline VDI/VDE 2630 1.3 [32] as it should be applicable also for testing by the CT manufacturer and stating the MPE values.

Chapter 6

Simulation study on geometrical misalignments

The results of CT scan simulations with misaligned components were evaluated to examine the effects of geometrical misalignments on CT dimensional measurements. Misalignment of a real CT system would be challenging task requiring extensive intervention to CT hardware. Performing simulations is more suitable for this kind of study as it allows us to efficiently perform multiple CT scans at a reasonable time without risk of damaging expensive CT hardware. The benefit of simulation is that we can avoid other error sources, such as uncertainty of reference object calibration, which would be present in real CT scan and focus only on the system geometry, which can be set exactly.

The presented study aims to give an extensive overview of all possible misalignments and their effects on dimensional measurements and determine which factors have the most significant impact. Such summarizing work is currently missing in this field. Effect of linear shifts in x, y and z-axis and angular misalignments φ, ϑ and η of detector and rotation stage were tested with magnitudes which can appear in common practice (order of $0.1\,^\circ$ and 0.1 mm presented e.g. in [34]).

Unidirectional measurements are suitable to access the errors of dimensional from system geometry and avoid other error sources. Therefore a ball plated is utilized as a reference object, and the errors between the sphere centers S_D are analyzed. It is useful to analyze as well as probing errors P_S and P_F as they are associated with image artifacts caused by some of the misalignments. Previous studies show that errors are not homogeneous over the entire measured volume. Distances between the spheres are categorized in groups according to their position and direction in measured volume to investigate the spatial and directional distribution of the errors.

6.1 Objectives of the study

We will determine influence of misalignments of detector, which are out-of-plane rotations (tilt ϑ and slant φ), in-plane rotation (skew η), linear shift x_d, y_d and z_d, and rotation axis tilt ϑ_r, skew η_r and shift in x- and y-direction. All examined values of misalignments are shown in Table 6.1.

Table 6.1: Tested values of misalignments

Detector misalignments											
x_d [mm]	+0.1	−0.1	+0.2	−0.2	+0.3	−0.3					
x_d [mm][1]	+0.1	+0.3									
y_d [mm]	+0.1	−0.1	+0.2	−0.2	+0.3	−0.3					
z_d [mm]	+0.01	−0.01	+0.03	−0.03	+0.05	−0.05	+0.5				
ϑ [°]	0.01	0.02	0.03	0.05	0.1	0.2	0.3	0.4	0.5[3]	1.0[3]	1.5[3]
φ [°]	0.1	0.2	0.3	0.4	0.5[3]	0.6	0.74	1.0[3]	1.5[3]		
η [°]	0.5[3]	1.0[3]	1.5[3]	2	2.5						
η [°][2]	0.05	0.075	0.1	0.2	0.3	0.4					
Rotation axis misalignmentds											
x_r [mm]	+0.3	−0.3	+0.5	−3							
x_r [mm][1]	+0.02	+0.03	+0.04	+0.05	+0.1						
ϑ_r [°]	0.01	0.02	0.05	0.1	0.2	0.3	0.4	0.5	1.0	1.5	
η_r [°]	0.5	1.0	1.5								
η_r [°][2]	0.05	0.075	0.1	0.2	0.3	0.4					

Additionally, the effect of different magnification was examined on simulations with aligned detector, with slant $\varphi = 0.6\,°$, tilt $\vartheta = 0.03\,°$, $\vartheta = 0.05\,°$ and $\vartheta = 0.1\,°$. CT simulations of these misalignments were performed with voxel size 20, 30, 40 and 50 µm. Magnification was changed by moving the sample closer to the detector to $SRD = 117.6, 176.4, 235.2,$ and 294.0 mm respectively.

6.2 Methodics of the simulation processing

6.2.1 Simulation parameters

Simulations were performed in software aRTist 2.10 (BAM, Germany). This software uses a ray-tracing model based on Lambert-Beer law to simulate the acquisition of tomographic projections. It allows us to set geometric parameters of the acquisition (position and orientation of the source, sample, and detector) and settings of the X-ray tube and detector parameters [35]. Simulations with detector misalignment were performed using aRTist module CTScan. To simulate a CT scan with a misaligned rotation axis, module Tomosynth was used as it allows more extensive scanning trajectory settings.

Scan simulations were performed by the circular trajectory with 1000 projections per revolution. Setup parameters were chosen to correspond with real metrological CT system. The detector has pixel size $p = 0.02$ mm and resolution 2024×2024. X-ray spectrum was simulated for a reflexive X-ray tube with a tungsten target, voltage 110 kV and aluminum filtering of the beam. Reconstructed volume has voxel size $(20\,\mu m)^3$ which was achieved by setting the SDD to 1176 mm and SRD to 117.6 mm.

[1] Without rotation axis determination during reconstruction

[2] With only single slice rotation axis determination during reconstruction

[3] Results from simulations of these misalignments were already presented by Sbettega et. al. [5]. They are included in this study with courtesy of author.

6.2.2 Reference object

The object used for dimensional analysis was a carbon fiber plate with 56 ruby spheres distributed in 7×7 grid and chosen interstitial position. 347 distances from 5 to 42.4 mm were evaluated in 6 spatial directions. Previous studies showed that errors caused by misalignments are not always homogeneous over the entire volume. To evaluate the effect of misalignments in different regions of the measured space, we will distinguish errors of the distances between the spheres based on the position and on the orientation of their connecting line. Distance between spheres in horizontal and vertical direction will be taken into account and categorized in groups X1...X7 and Y1...Y7, respectively (Figure 6.1), to show the differences between regions of measured volume. All analyzed distances (labeled by pairs of numbers corresponding to included spheres) and their categorization are defined in Table A.1. To make the orientation in results simpler we will present mainly the errors corresponding to distance groups X1 (top row), X4 (middle row), X7 (bottom row), Y1 (left column), Y4 (middle column), Y7 (right column).

The ball plate was positioned in the measured volume with middle column (Y4) lying on rotation axis and sphere 25 on the line from the source to the middle of the detector.

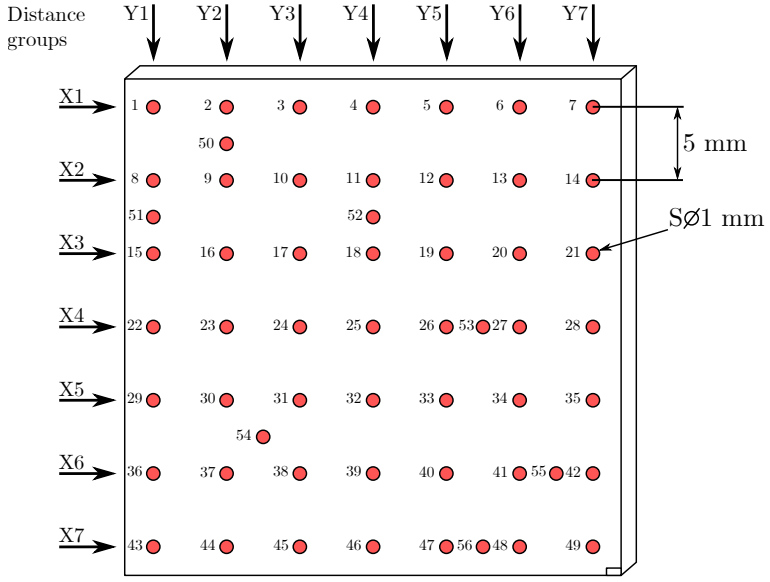

Figure 6.1: Ball plate tomographic cross-section with the numbering of spheres and labels for the groups of distances which will be used for evaluation of effects in a measured volume

6.2.3 Reconstruction and postprocessing

Data were reconstructed by a commercially available reconstruction software CTPro 3D (Nikon Metrology, UK). One of the functions of this software is a determination of the position of the rotation axis based on the analysis of one or two slices of the to-be-reconstructed volume. It allows to compensate detector or rotation axis shift in x-direction or skew (η, η_r) in case of two-slices determination. Analysis was by default performed with two-slice determination. However, to analyse effect of skew and shift in x-direction only one-slice determination was used. Reconstruction was performed in 16bits.

Analysis of reconstructed data was performed using VGStudio MAX 3.2. (Volume Graphics GmbH, Germany). Procedure was performed as follows:

- Creating region of interests which contains only spheres and excludes part of the volume with base plate.

- Extracting the region of interest as separate volume and determination surface. Automatic threshold (ISO 50%) with advanced (local) thresholding (search distance 4 voxels is selected).

- Spheres n. 1, 7 and 43 are manually fitted on the surface (at least 5 points are selected in the top hemisphere, avoiding area around poles). Lines from spheres 1-7 and 7-43 and plane from all 3 spheres are created.

- Volume is registered using 3-2-1 registration. Normal to plane is chosen as main axis, with positive orientation in z direction and as the origin coordinate z. Line 1-7 is chose as auxiliary axis, with positive orientation in x direction and as the origin of coordinate y. The center of the sphere 1 is set as origin of coordinate system.

- Center-to-center distances, sphere diameter and sphere form are calculated. Data are exported as .csv file.

In the analysis, three parameters defined in section 4 were taken into account: S_{D}, P_{S} and P_{F}. The distances between the sphere centers and diameters of the spheres obtained with the simulation of the aligned system were used as a reference. Main focus is put on error S_{D} which is not significantly influenced by thresholding and other error sources, therefore are suitable for analysis of geometrical errors, for example unhomogeneous magnification over the measured volume. Analysis of form errors is useful because these errors are associated with image artifacts, which cause misshaping of spheres in CT volume. This happens eg. due to detector skew. Sphere diameter error corresponds to magnification errors similar as center-to-center distances, but they are influenced by thresholding method, image artifacts etc. Even for aligned scan, diameters have systematic deviation from nominal value (1 mm) about 2.4 µm. However we use results of first aligned measurement as reference so we do not deal with this default systematic error here.

6.3 Accuracy of the simulation approach

To know how accurate the used simulation setup with subsequent analysis is and how large the smallest possibly detectable errors are, 10 simulations with aligned system were performed and evaluated. Highest registered error S_{D} (using a one aligned scan as reference) was 1 µm. Error of spheres form P_{F} varies from 9.4 (at sphere n. 21) to 17.5 µm (at corner sphere n. 7). Deviations from nominal diameter P_{S} varies from 1.6 to 3.2 µm. Highest deviation of ball diameter from reference simulation is 0.8 µm. Measured errors under these values are considered negligible in this study, as is summarized in Table 6.2.

Table 6.2: Error values chosen as significant for the purpose of the study. Obtained errors under these limits will be considered negligible.

	S_{D}	P_{S}	P_{F}
Limit values	1 µm	0.8 µm	17.5 µm

6.4 Results of simulations with misaligned components

The simulations were performed with described parameters for all magnitudes of misalignments mentioned in Table 6.1. In this section results for every misalignment will be sumarized.

6.4.1 Detector misalignments

x_d Detector shift is one of the misalignments which is easily corrected by used reconstruction software even for highest tested values. Repeated reconstructions without rotation axis determination for values up to 0.3 mm also did not resulted in errors higher than 1 µm so we can consider them negligible.

y_d Shift of detector in y direction also did not caused any significant errors of dimensional measurements for tested values up to 0.3 mm.

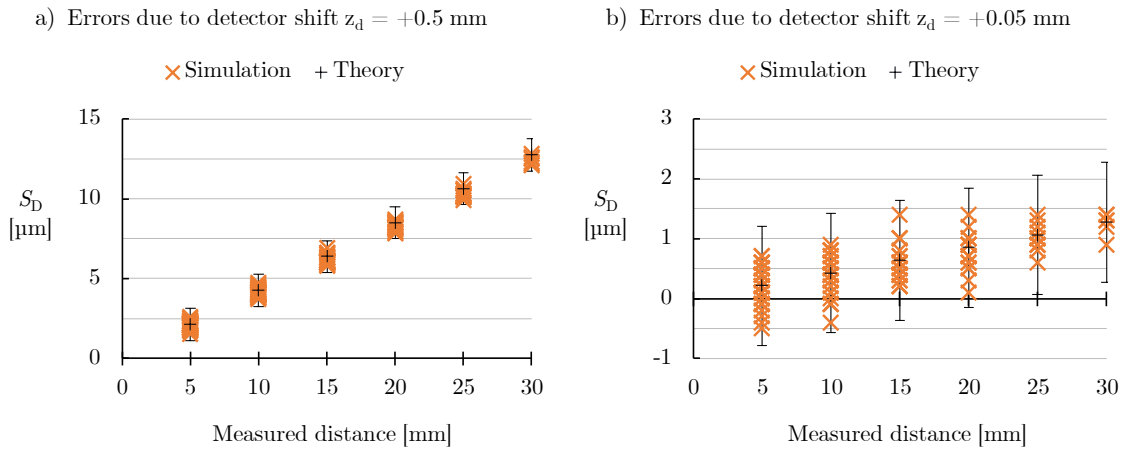

Figure 6.2: Errors in both x- and y-direction increases with z_d. All errors correspond to theoretically determined values within the accuracy interval of simulations (error bar length is 1 µm).

z_d Shift of detector in z-direction had direct effect on magnification and thus on all dimensions. Results from simulations showed that all errors correspond with theoretically determined values according to 3.2 as can be seen in Figure 6.2 taking into account the accuracy of simulations. Magnitude of errors is linearly dependent on measured distance. The slope of the errors increases with the detector shift.

ϑ Tilt of the detector has impact on dimensional measurements in all directions and on balls diameter determination. Critical value, when S_D errors raise above limits is $\vartheta = 0.01\,°$. The effect on distances depends on their position in the field of view and is different for x- and y-direction. Distances in x-direction at the top row (X1) have negative error, at the bottom row (X7) positive error, in the middle row (X4) the errors are negligible. It can be explained by the fact that due to the detector tilt, the top part is displayed with a higher magnification thus the distances are smaller. In the bottom part, the magnification is bigger and in the middle part the magnification does

not change. The effect is stronger with the increased magnitude of the misalignment, as is clear from the left chart in the Figure 6.3.

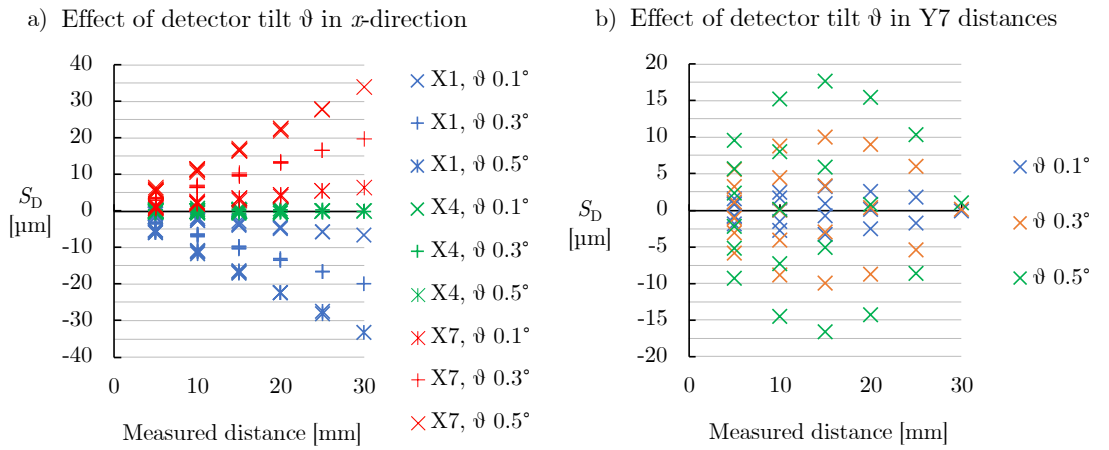

Figure 6.3: Errors of chosen distance groups in a) x- and b) y-direction for the tilt ϑ of the detector.

Errors in y-direction show different behavior. The largest and smallest distances have small errors around 0. That is because positive error in bottom part is compensated by negative error in the top. The highest errors appear for distances which are only in the bottom or the top part (eg. distances 7-28 or 28-49). Errors are equivalent for all columns, so results in right chart in Figure 6.3 are shown only for distance group Y7.

Difference in error magnitudes for different directions caused by detector tilt are illustrated in the right chart in the Figure 6.4. It can be estimated, that errors increase linearly depending on the tilt angle magnitude. Errors are summarized in the Table B.2.

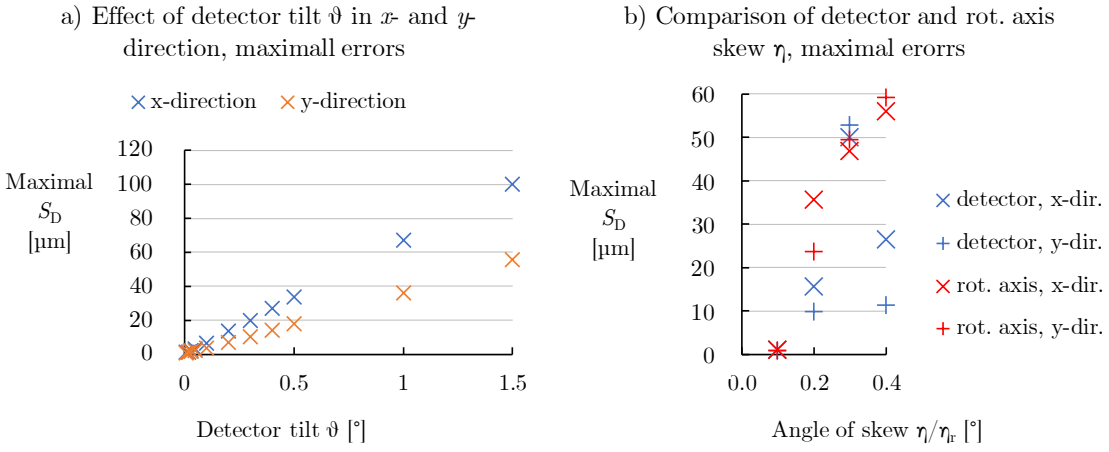

Figure 6.4: Maximum S_D errors due to detector a) tilt and b) skew in x- and y-direction

φ Slant of the detector has large impact on distances in x-direction, it causes positive error. Errors increase linearly with measured distance with slope increasing with slant

magnitude. Effect starts to be significant at slant $\varphi = 0.4\,°$. Effect on y-direction is significantly smaller compared to the x-direction. Positive errors above 1 µm in the absolute value starts to occur at slant $\varphi = 1\,°$. Results are shown in Figure 6.5 and in Table B.3. Detector slant has also impact on errors of form and diameter errors of spheres. Errors increase mainly with distance form center in x-direction. Detail of artifact on one of the corner spheres (43), where it is most significant at slant $\varphi = 1.5\,°$, is shown in Figure 6.6.

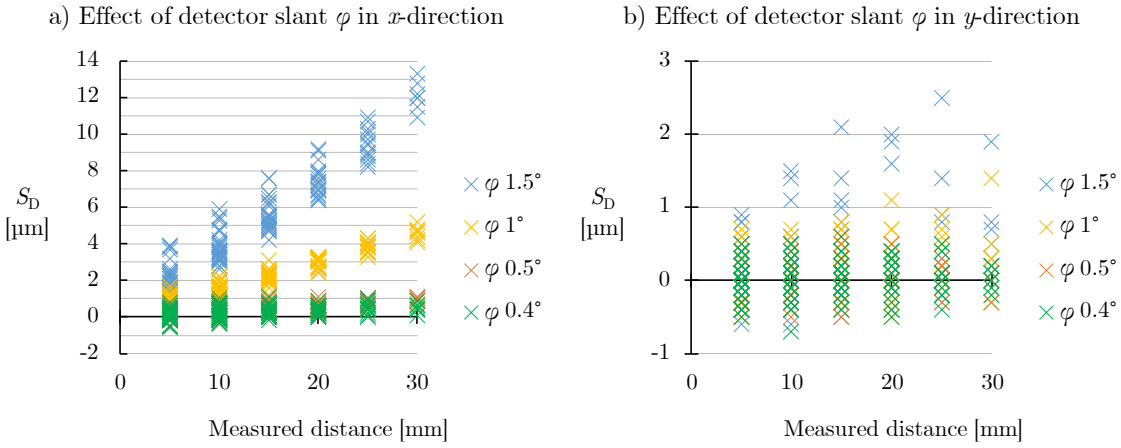

Figure 6.5: Errors in a) x- and b) y-direction for the slant φ of the detector

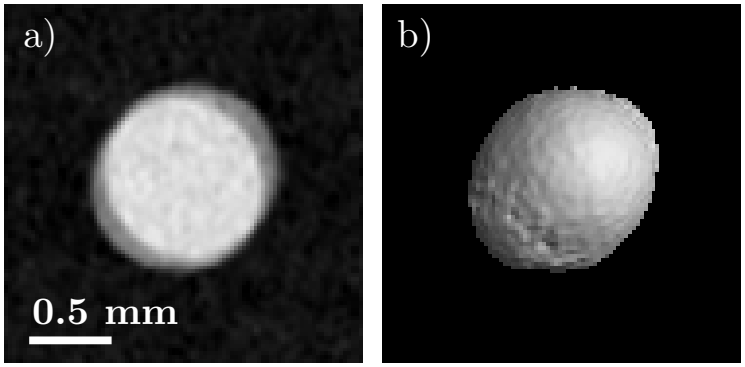

Figure 6.6: Blurring of sphere edges due to detector slant from angle $\varphi = 1.5°$. Image a) shows a tomographic cross-section of corner sphere number 7, the image b) shows a 3D render.

η Skew of the detector (in-plane rotation) is easily compensated by reconstruction software. Software is able to determine shift of rotation axis in two different slices and from this deduce its skew. All tested skew values were compensated so errors were negligible.

Simulations of skew were repeated for lower magnitudes of skew and with determination of rotation axis using only one slice (in the middle of field of view). In this case critical angle is $\eta = 0.1\,^{\circ}$, where errors in group of distances X1 increase above limits. Skew of detector causes artifacts in CT data. Sphere object is reconstructed as two overlapping sphere objects, each individually having a lower material attenuation value than the overlapping section [24] (see Figure 6.7). This causes probing errors of form and size, complicates fitting of sphere and thus causes high deviation in spheres center position which directly influences distances measurement. This artifact is stronger with the distance from the center of measurement volume (which corresponds to the center of the detector in projections) where the linear shift of pixels is higher. Dimensional errors can highly increase if the distances include a sphere which si more damaged by the artifact.

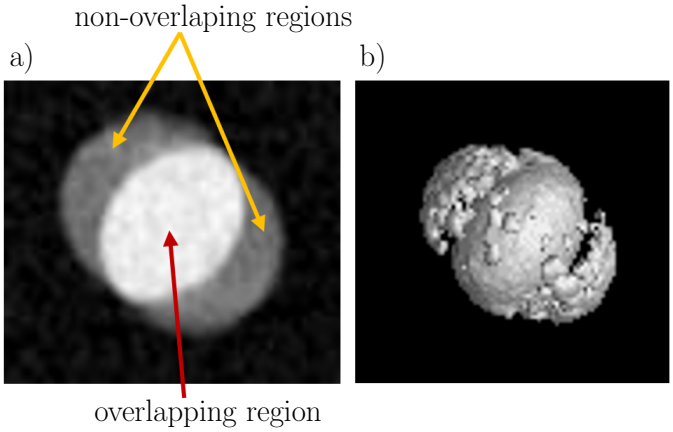

Figure 6.7: Artifacts due to detector skew (for $\vartheta = 0.4°$) in corner sphere n. 43. Part a) shows a cross-section with marked overlapping and non-overlapping regions. Part b) shows 3D render with clearly visible form deviations.

A noteworthy fact is that maximal distance errors for angle of 0.4° are smaller than for angle 0.3° as is visible in chart on Figure 6.8. Sphere center determination is here affected mainly by image artifacts, surface determination and sphere fitting method. In this case only the overlapping region in segmented as the sphere surface for lower amplitudes of skew and in case of higher amplitudes the non-overlapping regions are segmented. Segmentation of also non-overlapping regions results in better determination of the sphere center and so lower S_{D} errors.

6.4.2 Rotation axis misalignments

x_{r} Rotation axis shift in x-direction is easily avoided by reconstruction software in the same way as detector shift and skew, and hence, in this case has a negligible effect.

Simulations with values of x_{r} from 0.02 mm to 0.1 mm were performed without rotation axis determination during reconstruction. Errors raise above limits at $x_{\mathrm{r}} =$

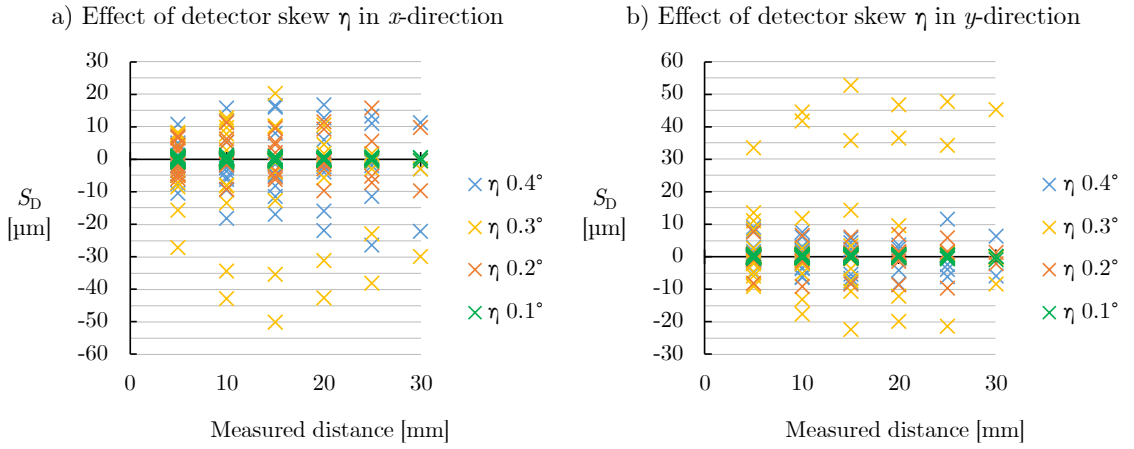

Figure 6.8: Errors in a) x- and b) y-direction for the skew η of the detector

$= 0.02\,\mathrm{mm}$. This misalignment causes artifacts similar as due to detector skew, however, the overlapping circles in image are oriented in x-direction. Artifacts are homogeneous over the volume as is visible in Figure 6.9. This corresponds with the fact that the distance errors are many times higher in x direction than in y-direction as is visible on charts in Figure 6.10. For the highest tested value of $x_\mathrm{r} = 0.1\,\mathrm{mm}$ the maximum error in x-direction is $23\,\mu\mathrm{m}$, which is about six times higher than the maximum error in y-direction, which is $4\,\mu\mathrm{m}$.

Overview of results is given in the Table B.5.

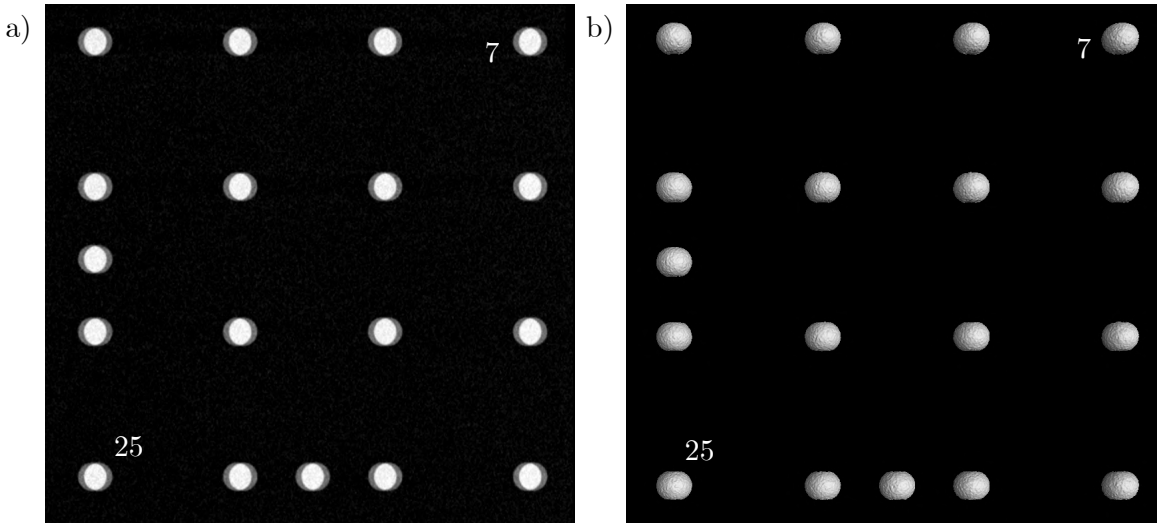

Figure 6.9: Blurring of sphere edges due to rotation axis shift x_r does not depend on sphere position. Image shows the top right corner of the ball plate delimited by the spheres 7 and 25. Results of the reconstruction without rotation axis determination: a) tomographic cross-section, b) 3D render.

ϑ_r Tilt of rotation axis has high impact on measurement accuracy. It causes images artifacts on spheres in form of two overlaping circles (shown in Figure 6.11) and

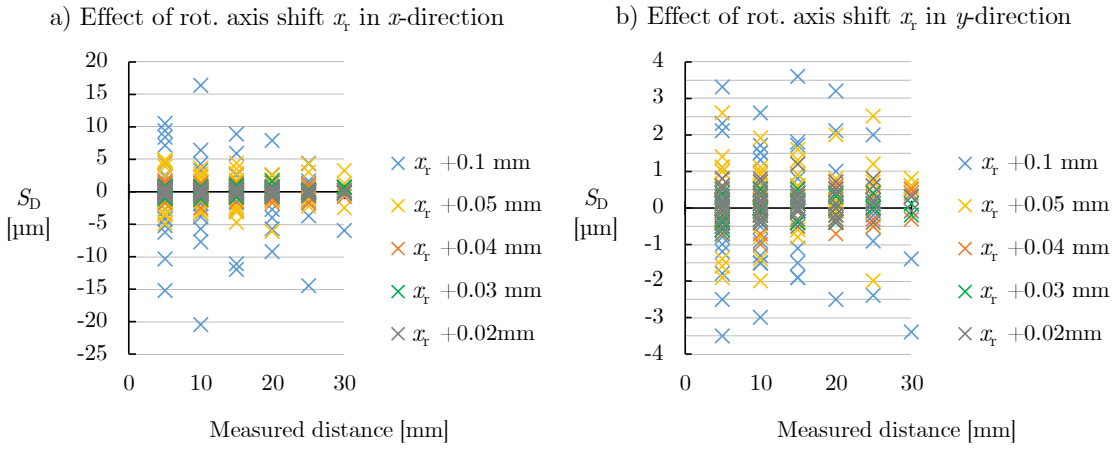

Figure 6.10: Errors due to the shift x_r of the rotation axis from 0.02 mm to 0.1 mm. Errors in x-direction (a) are higher than in y-direction (b).

inhomogeneous magnification similar as tilt of detector. Figure 6.12 shows that errors are for the same magnitude of the tilt smaller than for the tilt of the detector. It should be noted, that effect on top and bottom of the measured volume is inverse for tilt of the rotation axis. Overview of rot. axis tilt errors is shown in Table B.6.

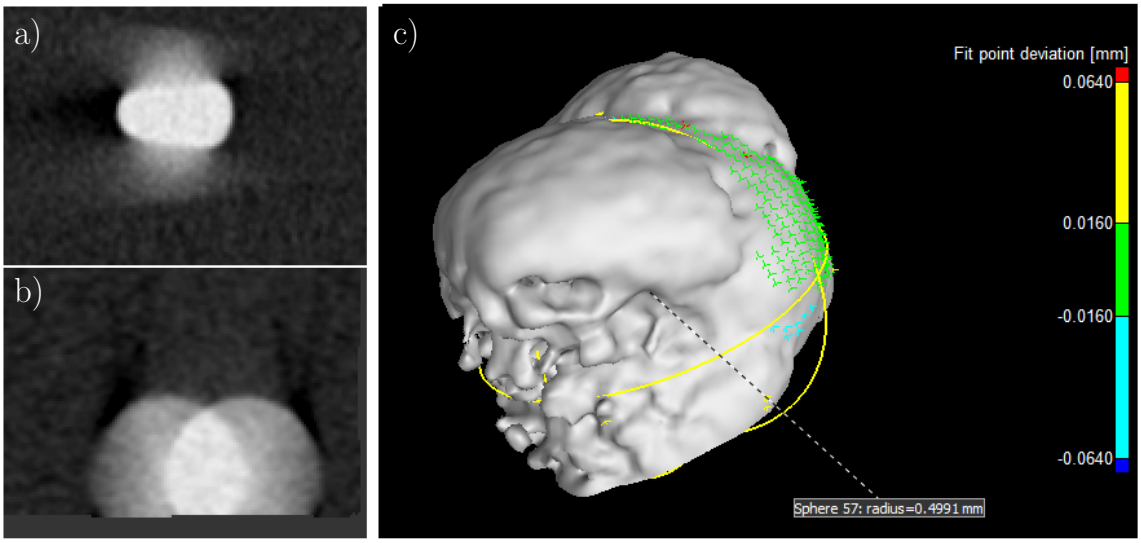

Figure 6.11: Artifacts due to rotation axis tilt (for $\vartheta_r = 1°$). The left part shows a cross-section of corner sphere from a) top and b) side view. The right part c) shows 3D render with clearly visible form deviations.

η_r Skew of rotation axis is easily compensated by reconstruction software, even for higher angles. Simulations for angles from 0.05° to 0.4° were performed with the determination of the rotation axis position only in the middle slice. Effect of rotation axis skew is similar to detector skew, both cause artifact of sphere's form, which has effect also on dimensional measurements. Figure 6.13 shows that errors caused by skew

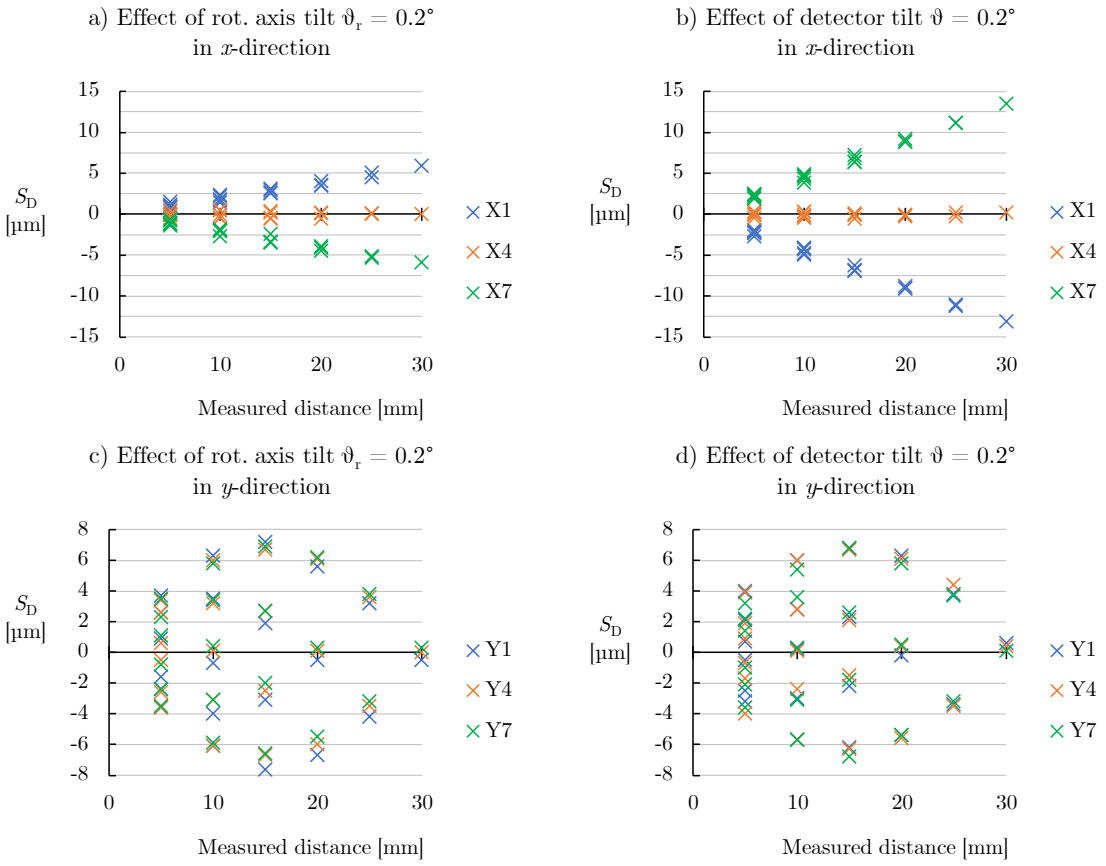

Figure 6.12: Comparison of errors for detector tilt $\vartheta = 0.2\,°$ (a, c) and rotation axis tilt $\vartheta_r = 0.2\,°$ (b, d) in x- and y-direction.

of the rot. axis are slightly larger than those caused by the detector skew for same magnitudes. The effect is not more significant in any direction, but higher errors are associated with spheres located farther from the center of rotation. Maximal errors overview for tested angles is shown in Table B.7.

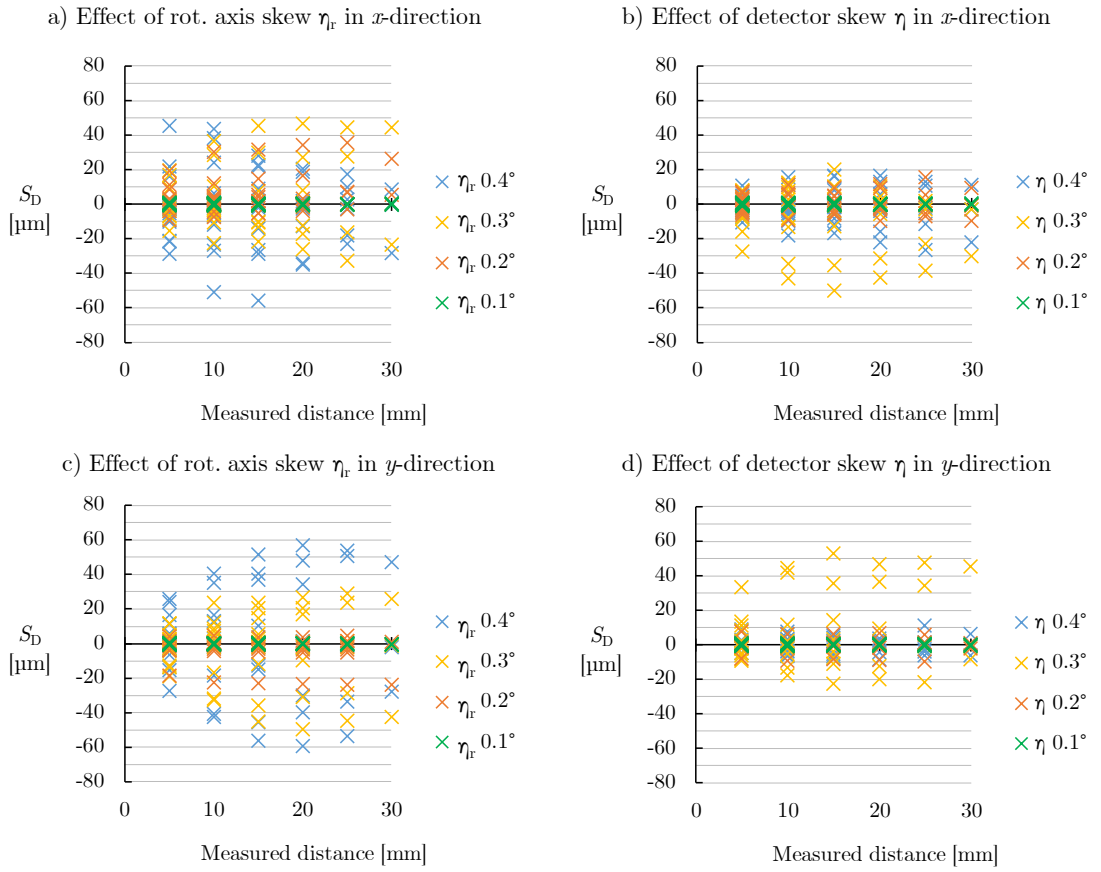

Figure 6.13: Comparison between the effects of rotation axis skew η_r (a, c) and detector skew η (b, d) from 0.1° to 0.4° for x- and y-direction. Slightly larger errors were detected for η_r.

6.4.3 Effect of different magnification

Decreasing magnification affects the accuracy of the measurements, as it decreases effective resolution of the measurement which has also effect on slight increase of errors, as is show on top left chart in Figure 6.14 for aligned scan. For small magnitudes of misalignments as detector slant $\varphi = 0.6°$, the effect of decreased magnification is not significant (see the bottom right chart in Figure 6.14). However, for higher magnitudes of misalignments which cause higher errors, we can observe that errors are decreased for higher voxel size. Comparison in the bottom left chart shows that errors for detector tilt $\vartheta = 0.1\,°$ are approximately two-times lower for linear voxel size 40 µm, which corresponds to the fact, that sample is imaged with half magnification.

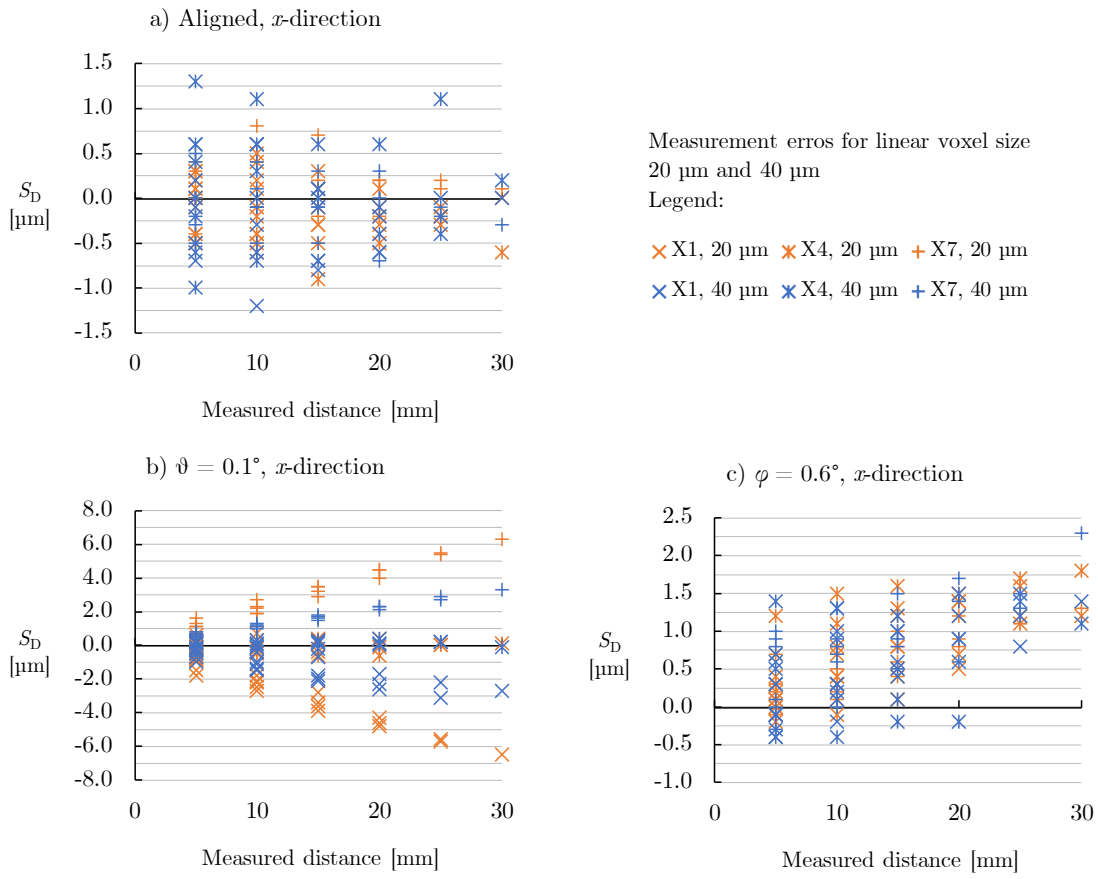

Figure 6.14: Errors for a) aligned scan, b) detector tilt $\vartheta = 0.1\,^\circ$ and c) detector slant $\varphi = 0.6^\circ$ in x-direction. Comparison for linear voxel size 20 and 40 µm.

6.5 Discussion

In this work, simulation study of geometrical misalignments effect on CT dimensional measurements was performed. It covers detector and rotation axis angular and linear misalignments and determines their impact on dimensional measurements. Therefore, it gives an almost full overview of possible misalignments and their impact (it does not cover errors of the rotation axis angular index and planar distortions of the detector).

Most critical found misalignment is detector tilt ϑ; it causes significant errors even for the smallest angle, which was possible to set in the simulation software (0.01°). Another critical misalignment is tilt of rotation axis ϑ_r, which causes not only distance errors but also artifacts of spheres form. Relevant error sources are also detector and rotation axis skew (η, η_r) and shift in x-direction (x_r), which causes reconstruction artifacts on spheres form. But they can be easily compensated by commercially available reconstruction software, which can determine the actual position of the rotation axis.

The effect of different magnification was observed by repeating chosen misalignments simulations with the object moved closer to the detector (increasing voxel size). Decreasing magnification causes decreasing precision of measurement (higher random errors in aligned measurement). It also reduces the magnitude of distance errors caused by misalignment.

In general, effects of singular misalignments correspond with results in previous studies [24, 26] in trends of errors (specific values may differ due to differences in used models, e.g. system geometry) and other effects (image artifacts on spheres). Our study shows variations of the behavior of the detector tilt and slant in a circular cone-beam CT measurement; x- and y-direction errors were different. Kumar et. al [23] showed similar behavior for errors in both directions. This difference could be explained by excessive simplification of Kumar's study and not so distinct visualization of results in charts so that errors in all directions and positions were not distinguishable.

Chapter 7

New reference objects for calibration and error evaluation

Results presented in the previous chapter confirmed that misaligned geometry of the CT system causes measurement errors. Methods which can be used to reduce the effect of this error source were introduced in section 3.3. To obtain high-quality measurements, every manufacturer of CT systems has to implement methods of system geometry corrrection introduced in section 3.3. It is necessary mainly when performing dimensional measurements on the CT data. We will use one of CT devices located in the laboratory, Heliscan. HeliScan uses a unique calibration approach which is based only on measured data itself and can correct scale errors as well as other linear and angular misalignments of detector. We will introduce new reference object suitable for testing of metrological performance of this system.

7.1 HeliScan microCT device

HeliScan is a X-ray micro-tomography system manufactured by Thermo Fisher Scientific company.

It features transmissive X-ray tube with a tungsten target able to operate from 20 to 160 kV with maximum power 8 W. X-ray detector is a flat panel with resolution 3072×3072 pixels, pixel pitch 139 µm and 16 bit dynamic range. The kinematic system allows movement of the detector and rotation stage in z-axis to adjust magnification and cone beam angle and movement of the rotating stage in y-axis allowing helical scanning. The detector can be shifted by purpose in x-direction to reduce image artifacts.

7.1.1 Operating modes

HeliScan can operate in a circular cone beam configuration as most industrial CT systems and helical trajectory with double-helix or so-called space-filling mode. The circular trajectory is based on projections acquisition of the sample rotating through 360 degrees with a fixed vertical position. A drawback of this configuration on the device is that small cone beam angles (less than 10°) are allowed to avoid cone-beam artifacts. Cone angle can be decreased either by cropping the FOV on detector or moving detector further from the source which means to increase the exposure time to obtain sufficient intensity on the detector plane.

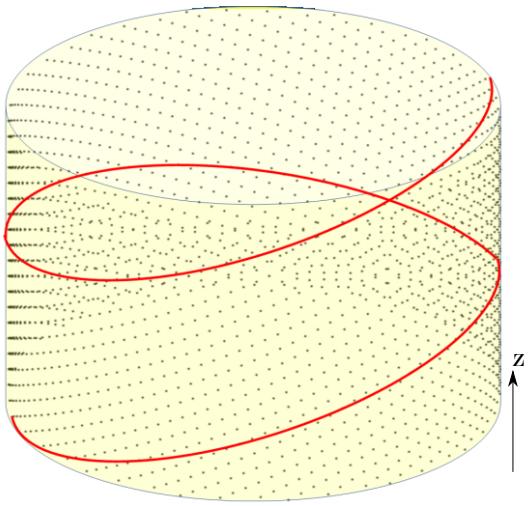

Figure 7.1: Schematic visualization of the X-ray beam trajectory with respect to the measured sample (yellow cylinder). The red line represents helical scan which is acquired in a continuous trajectory curve with a progressive increment of the rotation angle and vertical travel. Grey dots represent space-filling trajectory where projections are widely spread around the sample. (Thermo Fisher Scientific Inc. [36]).

For tall samples is better to use helical trajectory when the sample is simultaneously rotated and moved up to the next position where X-ray projection is acquired. Double-helix trajectory with reconstruction based on FBP algorithm consists of two single helical scans that are performed with starting position rotated 180 degrees apart. In this configuration, detector can be moved closer to the source utilizing more X-ray flux (better signal-to-noise ration). As every point of the reconstructed volume traveled trough the detector midplane it allows theoretically exact reconstruction (distortion-free). This approach is suitable for scanning of tall samples reducing the total measurement time compared to the stitching of multiple measurement volumes scanned using circular trajectory [36].

HeliScan microCT provides as well the space-filling trajectory with iterative reconstruction which improves the uniformity of the sampling and allows optimization of measurement time by utilizing full detector area, reducing over-scan and allowing higher cone-angle imaging [37]. Difference between classical helix and space-filling trajectory is depicted in Figure 7.1, space-filling trajecotry projections are more uniformly spread over the entire measured volume.

7.1.2 Calibration method

To obtain high-quality data, HeliScan uses an autofocus algorithm to determine SDD, SRD, detector tilt ϑ, slant φ and skew η, shift in x- and y-axis and corrects for drift caused by spot or sample movement [38, 8]. It performs this analysis on measured data itself without any other reference. This approach could be very promising as well for metrological analysis on CT data as it decreases uncertainty of the measurement while it does not rely on accurate and therefore expensive position system and avoids additional measurements of a reference object.

One of the critical point of this approach is that even in case of precise alignment of the obtained projections and determination of correct magnification (ratio $\frac{SRD}{SDD}$) the scale

of the reconstructed volume relies on the value of pixel size p, which therefore must be accurately stated. For the HeliScan detector used in this thesis, the manufacturer specifies $p = 139\,\mu\text{m}$, without the uncertainty statement.

7.2 Reference objects for calibration and verification of metrological performance

To verify the performance of HeliScan, with focus mainly on its unique reconstruction approach, new reference objects suitable for probing and length measurement errors based on the requirements of VDI/VDE 2630 1.3 [32] were developed. Method A of length measurement error evaluation was chosen due to its lower measurement time demands. The guideline explains method of verification of manufacturer specification. In the case of HeliScan, manufacturer does not specify any characteristics MPE. Detailed analysis of measurement errors using the newly developed reference objects may therefore serve the manufacturer of the HeliScan to state the MPE values in agreement with the VDI/VDE 2630 1.3.

A common design of a plate with ruby spheres was adapted to comply with requirements of guideline to evaluate S_{D}. Ball plate is designed in two versions - large one for low resolution and large FOV imaging with highest measured length 35 mm and small one for high resolution and small FOV imaging with the highest measured length 17.5 mm, to be able to evaluate performance in two magnifications. Spheres are distributed in special pattern so that distance between spheres can be evaluated in 7 spatial directions. For probing error evaluation is suggested to use a calibrated sphere with diameter corresponding to 10-20% of a ball plate measurement space diagonal.

First, the objects for evaluation in larger FOV will be introduced and tested. The design of objects suitable for smaller FOV will be introduced drawing on the experience with larger objects testing.

7.2.1 Large FOV evaluation

Design and manufacture of the objects for large FOV

Design of the large phantom is depicted in Figure 7.2 a). The dimensions were chosen to fit in the FOV which allows CT scans with linear voxel size approximately 15 µm. Polycarbonate plate of 2 mm thickness was used as the base. The material was chosen due to its low density and high permeability for X-rays. Advantage of the polycarbonate is its transparency for visible light which allows to perform calibration using coordinate measuring machine with an optical sensor.

Ruby spheres were precisely positioned according to the drawing (C.1) and glued with epoxy resin on the plate. Ruby is one of the hardest materials and due to its stability is commonly used in metrological applications in form of precision spheres, which features low surface roughness and high sphericity [39].

Single zircon sphere with nominal diameter 10 mm is used for accessing the probing errors P_{S} and P_{F}. Zircon is very tough ceramic material with similar properties as ruby, which makes it also very suitable form metrological applications [39]. Sphere is glued by epoxy resin on a carbon fiber rod which is fixed in specially designed holder allowing measuring in six different positions in agreement with the guideline. Design of the sphere and holder assembly is shown in Figure 7.2 b).

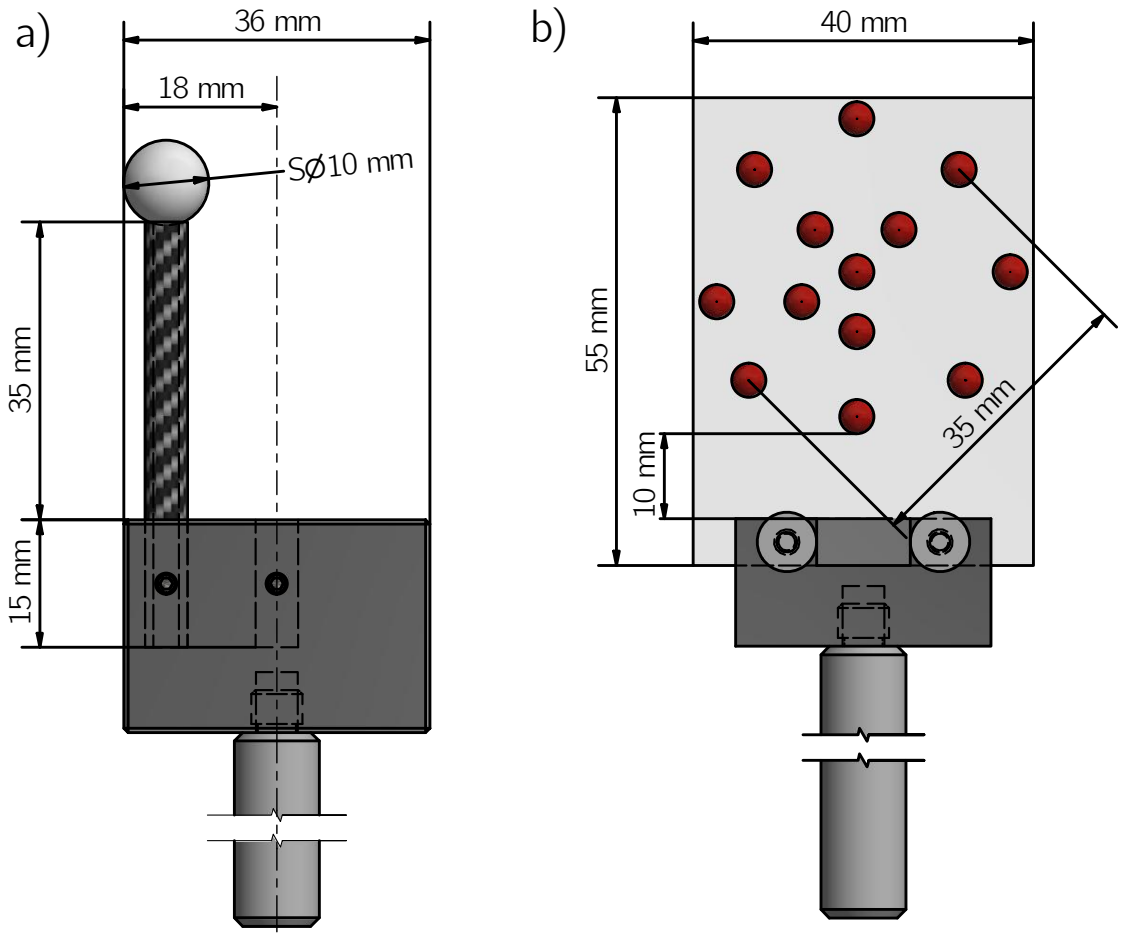

Figure 7.2: Design of a) ball plate and b) zirkon sphere assembly for HeliScan performance verification in large field of view.

Calibration of the objects for large FOV

Reference measurement of the ballplate was performed on optical coordinate measuring machine EXEL 4520, MicroVu. Advantage of optical approach compared to the tactile measurement is that no force is applied on the ball plate, which avoids the possibility of damage. Position of the sphere centers was measured in two axes, assuming that all spheres are in one plane. Distances were measured with expanded measurement uncertainty 0.001 mm (with coverage interval 95%, coverage factor $k = 2$). Measured coordinates are in calibration certificate C.3

Zircon sphere was calibrated using length measuring machine SIP 1002 M (SIP, Switzerland) and roundness meter TALYROND 595S Taylor Hobson, England) resulting in diameter $(10.0009 \pm 0.0005)\,\mu m$.

Testing of CT measurements of the objects for large FOV

The large version of the ballplate and zircon sphere was measured on HeliScan micro CT to test the abilities determination of the measurement errors according to the VDI/VDE 2630 1.3. Tests were performed with space-filling trajectory and magnification resulting at voxel size 14.6 µm, parameters are summarized in Table 7.1.

CT data of the ball plate was analyzed using macro in VGStudio Max 3.3. Local thresholding was applied to segment the surface of the spheres. CAD model was registered on the sphere surface by least squares method (*best fit*) to define the volume coordinate system. Measurement template was created to fit the spheres on the surface. Distances between the spheres were calculated and compared with the reference measurement. Sphere distance error S_D was calculated according to the definition 4.4. Results are shown in Figure 7.3

Table 7.1: Measurement parameters of the large ball plate and 10 mm zircon sphere scan

SRD	SDD	Voltage	Exposure	Skip	Average	Proj. per revolution	Filtering	Voxel size
40 mm	380 mm	100 kV	0.7 s	2	5	2880	0.2 mm SS [1]	14.6 µm

The zircon sphere was measured using the same parameters as the ball plate including the same setting of scan trajectory and total measurement volume size. Data was analyzed in VGStudio Max 3.3. applying local thresholding and smoothing for segmentation and linear regression was used for fitting the sphere on the segmented surface. The probing errors were then calculated according to 4.1 and 4.2 as $P_S = 0.28\,\mu m$ and $P_F = 14.57\,\mu m$.

Results from the first measurement of the ball plate show highest S_D value of 23 µm corresponding to measured distance 24 mm. Errors tend to positive values which indicate possibility of systematic deviation, which can be caused by thermal expansion, as the HeliScan does not have air conditioned cabinet, or inaccuracy of pixel size p.

Lenght measurement error E can than be obtained using results from both measurements according to 4.5. It is suggested to perform repeated measurement on longer period of time together with smaller version of the phantom co check for the temporal stability of the system so that MPE value can be responsibly stated.

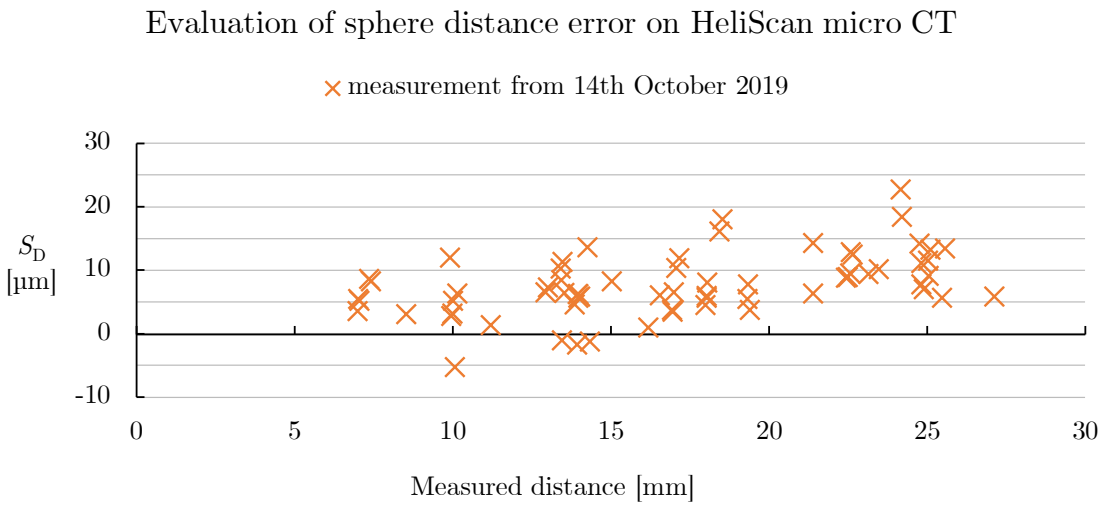

Figure 7.3: Result of the large ball plate measurement of HeliScan. Sphere distance error is shown depending on measured distance.

7.2.2 Small FOV evaluation

To fulfill the condition of the VDI/VDE 2630 1.3, second smaller version of the phantom suitable for scanning with higher resolution and smaller FOV is designed. It is suggested to use 3.5 mm thick carbon fibre composite sheet as a base. The material was chosen to improve stability of the phantom, while still being highly penetrable for X-rays. The material is not transparent for the visible light, however, it increases the stiffens of the phantom. It allows to calibrate it using more accurate tactile methods which can decrease the uncertainty of calibration measurement to 0.1 µm. Ruby spheres are positioned in a similar pattern as in the larger phantom as is shown in Figure 7.4 b).

To access probing errors, the zircon sphere of diameter 5 mm is selected. New holder suitable for measured volume of small ballplate is designed; see Figure 7.4 a).

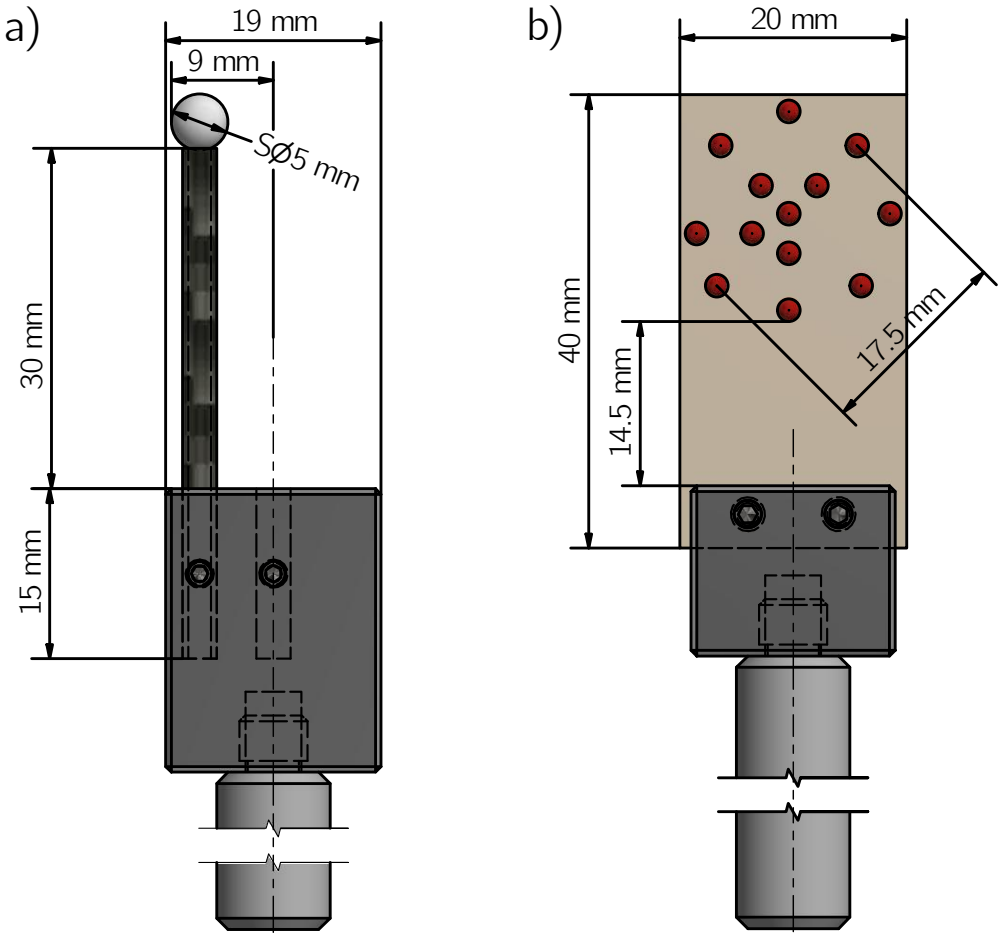

Figure 7.4: Design of a) ball plate and b) zirkon sphere assembly for HeliScan performance verification in small field of view.

Chapter 8

Conclusion

The simulation study presented in chapter 6 covered most of the critical factors and magnitudes of misalignments that are likely to appear during practical usage of CT systems in metrology. It was shown that the most critical source of errors is detector and rotation axis tilt $\vartheta, \vartheta_{\mathrm{r}}$ which causes significant errors even for the smallest analyzed amplitude of $0.01\,^{\circ}$ and cannot be avoided by used reconstruction software. It was also proven that angular misalignments tilt and slant have different effects depending on the position and direction of the measured distance. The repeated analysis of chosen misalignments with changed SRD showed that errors magnitude also depends on the CT setup magnification.

New reference objects were developed to test the abilities of online calibration methods implemented in HeliScan microCT to eliminate such errors. First, objects suitable for lower resolution measurements of probing and length measurement error were manufactured and calibrated, and the first results of HeliScan testing are presented. The highest recorded error of distances between the ballplate spheres is $23\,\mu\mathrm{m}$ for a distance of $24\,\mathrm{mm}$. The objects suitable for measurements with higher resolution is designed and will be manufactured and calibrated in a near future. These objects can be used for evaluation of measurement errors according to the German guideline VDI/VDE 2630 1.3. We suggest performing repeated measurement of these reference objects over an extended period and analyze the results to state maximum permissible errors (MPE) of length measurement on the device.

Bibliography

[1] Stock, S. R. *MicroComputed Tomography: Methodology and Applications*. CRC Press, 2008. 348 p. ISBN 9783642253874. Available at: 10.1201/9780429186745.

[2] De Chiffre, L., Carmignato, S., KRUTH, J.-P., Schmitt, R. and Weckenmann, A. Industrial applications of computed tomography. *CIRP Annals - Manufacturing Technology*. CIRP. jan 2014, vol. 63, no. 2, p. 655–677. DOI: 10.1016/j.cirp.2014.05.011. ISSN 17260604. Available at: https://www.sciencedirect.com/science/article/pii/S0007850614001930http://dx.doi.org/10.1016/j.cirp.2014.05.011.

[3] Ferrucci, M., Leach, R. K., Giusca, C., Carmignato, S. and Dewulf, W. Towards geometrical calibration of x-ray computed tomography systems - A review. *Measurement Science and Technology*. Institute of Physics Publishing. sep 2015, vol. 26, no. 9. DOI: 10.1088/0957-0233/26/9/092003. ISSN 13616501.

[4] Carmignato, S., Dewulf, W. and Leach, R. *Industrial X-ray computed tomography*. Cham: Springer International Publishing, oct 2018. 1–369 p. ISBN 9783319595733. Available at: http://link.springer.com/10.1007/978-3-319-59573-3.

[5] Sbettega, E., Zanini, F. and Carmignato, S. Simulation-based sensitivity analysis of geometrical misalignments in X-raycomputed tomography systems for dimensional metrology – detector angular misalignments. In: *9th Conference on Industrial Computed Tomography iCT*. 2019, p. 2. Available at: https://www.ndt.net/article/ctc2019/papers/iCT2019{}Full{}paper{}141.pdf.

[6] Illemann, J., Bartscher, M. and Neuschaefer rube, U. An efficient procedure for traceable dimensional measurements and the characterization of industrial CT systems. *Digital Industrial Radiology and Computed Tomography*. 2015, June, p. 22–25. Available at: https://www.ndt.net/events/DIR2015/app/content/Paper/46{}Illemann.pdf.

[7] Ferrucci, M., Heřmánek, P., Ametova, E., Carmignato, S. and Dewulf, W. Measurement of the X-ray computed tomography instrument geometry by minimization of reprojection errors—Implementation on simulated data. *Precision Engineering*. 2018. DOI: 10.1016/j.precisioneng.2018.03.012. ISSN 01416359.

[8] Kingston, A. M., Sakellariou, A., Varslot, T., Myers, G. and Sheppard, A. Reliable automatic alignment of tomographic projection data by passive auto-focus. *Medical Physics*. 2011, vol. 38, no. 9, p. 4934–4945. DOI: 10.1118/1.3609096. ISSN 00942405. Available at: https://aapm.onlinelibrary.wiley.com/doi/abs/10.1118/1.3609096.

[9] Blažek, P. *Stanovení nejistoty měření průměru děr ocelových součástí pomocí rentgenové počítačové tomografie.* 2018. Dissertation. Brno University of Technology. ISBN 9780898714944.

[10] Hsieh, J. *Computed Tomography: Principles, Design, Artifacts, and Recent Advances.* 2 editionth ed. Hoboken, N.J. : Bellingham, Wash: Wiley, nov 2015. ISBN 978-0-470-56353-3.

[11] Holmes, K., Elkington, M. and Harris, P. *Clark's essential physics in imaging for radiographers.* CRC Press, oct 2013. 1–177 p. ISBN 9781444165036.

[12] Buzug, T. *Computed tomography: From photon statistics to modern cone-beam CT.* Springer, 2008. 1–521 p. ISBN 9783540394075.

[13] Bushberg, J. T., Seibert, J. A., Leidholdt, E. M., Boone, J. M. and Goldschmidt, E. J. The Essential Physics of Medical Imaging. *Medical Physics.* 2003, vol. 30, no. 7, p. 1936–1936. DOI: 10.1118/1.1585033. ISSN 0094-2405.

[14] Leroy, C. and Rancoita, P. G. *Principles of radiation interaction in matter and detection, third edition.* World Scientific Pub. Co, 2009. 1–1018 p. ISBN 9789814360524.

[15] Kalasová, D. *Využití fázového kontrastu v rentgenové počítačové tomografii.* 2016. 56 p. Diplomová práce. Vysoké učení technické v Brně. Fakulta strojního inženýrství.

[16] Cierniak, R. *X-ray computed tomography in biomedical engineering.* Springer London, 2011. 1–319 p. ISBN 9780857290267.

[17] Lifton, J. J. *The Influence of Scatter and Beam Hardening in X-ray Computed Tomography for Dimensional Metrology (Dissertation).* 2015. Dizertační práce. University of Southampton, Faculty of Engineering and the Environment, Electro-Mechanical Engineering Research Group.

[18] KRUTH, J.-P., Bartscher, M., Carmignato, S., Schmitt, R., De Chiffre, L. et al. Computed tomography for dimensional metrology. *CIRP Annals - Manufacturing Technology.* jan 2011, vol. 60, no. 2, p. 821–842. DOI: 10.1016/j.cirp.2011.05.006. ISSN 00078506.

[19] Müller, P. *Coordinate Metrology by Traceable Computed Tomography.* Kgs. Lyngby, 2013. Dissertation.

[20] Beuth Verlag GmbH. VDI/VDE 2630 Blatt 1.2 / Part 1.2. 2010, p. 35.

[21] Villarraga Gómez, H., Lee, C. B. and Smith, S. T. Dimensional metrology with X-ray CT: A comparison with CMM measurements on internal features and compliant structures. *Precision Engineering.* jan 2018, vol. 51, p. 291–307. DOI: 10.1016/j.precisioneng.2017.08.021. ISSN 01416359.

[22] Wenig, P. and Kasperl, S. Examination of the measurement uncertainty on dimensional measurements by X-ray computed tomography. *European Conference on Non-Destructive Testing.* 2006, p. 1–10.

[23] Kumar, J., Attridge, A., Wood, P. K. C. and Williams, M. A. *Analysis of the effect of cone-beam geometry and test object configuration on the measurement accuracy of a computed tomography scanner used for dimensional measurement.* IOP Publishing, mar 2011. DOI: 10.1088/0957-0233/22/3/035105. ISSN 13616501. Available at: http://stacks.iop.org/0957-0233/22/i=3/a=035105?key==crossref.16c53f8f093ddb1c3c1fc944dc3ddecf.

[24] Ferrucci, M., Ametova, E., Carmignato, S. and Dewulf, W. Evaluating the effects of detector angular misalignments on simulated computed tomography data. *Precision Engineering.* 2016, vol. 45, p. 230–241. DOI: 10.1016/j.precisioneng.2016.03.001. ISSN 01416359.

[25] Ferrucci, M. *Systematic approach to geometrical calibration of X-ray computed tomography instruments.* 2018. Dissertation. KU Leuven. Available at: https://lirias.kuleuven.be/2278520?limo=0.

[26] Aloisi, V., Carmignato, S., Schlecht, J., Ferley, E. and Savio, E. Experimental investigation on the influence of detector misalignment on X-ray CT measurement accuracy. In: *Proceedings of the 17th International Conference of the European Society for Precision Engineering and Nanotechnology, EUSPEN 2017.* 2017. ISBN 9780995775107.

[27] Ametova, E., Ferrucci, M., Chilingaryan, S. and Dewulf, W. A computationally inexpensive model for estimating dimensional measurement uncertainty due to x-ray computed tomography instrument misalignments. *Measurement Science and Technology.* Institute of Physics Publishing. apr 2018, vol. 29, no. 6. DOI: 10.1088/1361-6501/aab1a1. ISSN 13616501.

[28] Hiller, J., Maisl, M. and Reindl, L. M. Physical characterization and performance evaluation of an x-ray micro-computed tomography system for dimensional metrology applications. *Measurement Science and Technology.* IOP Publishing. aug 2012, vol. 23, no. 8, p. 85404. DOI: 10.1088/0957-0233/23/8/085404. ISSN 0957-0233. Available at: http://stacks.iop.org/0957-0233/23/i=8/a==085404?key=crossref.f16b74da17fdf2dcb54f5caf3bc9722e.

[29] Aloisi, V., Carmignato, S., Schlecht, J. and Ferley, E. Investigation on the effects of X-ray CT system geometrical misalignments on dimensional measurement errors. *ICT2017 7th confrence on industrial computed tomography.* 2017, iCT, p. 5–6.

[30] Lifton, J. J., Malcolm, A. A., Mcbride, J. W. and Cross, K. J. The Application of Voxel Size Correction in X-ray Computed Tomography for Dimensional Metrology. *Singapore International NDT Conference & Exhibition.* 2013, July, p. 19–20. Available at: https://www.semanticscholar.org/paper/The-Application-of-Voxel-Size-Correction-in-X-ray-Lifton-McBride/ae7929c9b4d89b77613bbe01d553cd2ab8619ef8.

[31] Illemann, J., Neuschaefer Rrube, U., Bartscher, M. and Bate, D. Determining spectrum-dependent source and detector positions in cone-beam CT. In: *8th Conference on Industrial Computed Tomography, Wels, Austria (iCT 2018).* 2018, iCT, p. 3–10. Available at: https://www.ndt.net/article/ctc2018/papers/ICT2018{}paper{}id163.pdf.

[32] Beuth Verlag GmbH. *VDI/VDE 2630 Blatt 1.3 / Part 1.3*. 2011.

[33] Bircher, B. A., Meli, F., Küng, A. and Thalmann, R. A geometry measurement system for a dimensional cone-beam CT. *ICT2018 8th confrence on industrial computed tomography*. 2018, iCT, p. 1–7.

[34] Dewulf, W., Ferrucci, M., Ametova, E., Heřmánek, P., Probst, G. et al. Enhanced dimensional measurement by fast determination and compensation of geometrical misalignments of X-ray computed tomography instruments. *CIRP Annals*. Elsevier USA. jan 2018, vol. 67, no. 1, p. 523–526. DOI: 10.1016/j.cirp.2018.04.124. ISSN 17260604.

[35] Bellon, C. and Jaenisch, G.-R. aRTist – Analytical RT Inspection Simulation Tool. *DIR 2007 - International Symposium on Digital industrial Radiology and Computed Tomography*. 2007, p. 25–28. Available at: `http://www.artist.bam.de/`.

[36] FEI Czech Republic. *HeliScan microCT User Manual*. Brno: [b.n.], 2018.

[37] Kingston, A. M., Myers, G. R., Latham, S. J., Recur, B., Li, H. et al. Space-Filling X-Ray Source Trajectories for Efficient Scanning in Large-Angle Cone-Beam Computed Tomography. *IEEE Transactions on Computational Imaging*. sep 2018, vol. 4, no. 3, p. 447–458. DOI: 10.1109/tci.2018.2841202. ISSN 2573-0436.

[38] Varslot, T., Kingston, A. M., Myers, G. and Sheppard, A. High-resolution helical cone-beam micro-CT with theoretically-exact reconstruction from experimental data. *Medical Physics*. oct 2011, vol. 38, no. 10, p. 5459–5476. DOI: 10.1118/1.3633900. ISSN 00942405.

[39] plc., R. *Materiály doteků*. 2020. Available at: `https://www.renishaw.cz/cs/materialy-doteku--6423`.

Appendix A

Tables

Table A.1: Distances between spheres in horizontal and vertical direction are categorized in groups X1 ... X7 and Y1 ... Y7.

X1	X2	X3	X4	X5	X6	X7	Y1	Y2	Y3	Y4	Y5	Y6	Y7
1-2	8-9	15-16	22-23	29-30	36-37	43-44	1-8	2-9	3-10	4-11	5-12	6-13	7-14
1-3	8-10	15-17	22-24	29-31	36-38	43-45	1-15	2-16	3-17	4-18	5-19	6-20	7-21
1-4	8-11	15-18	22-25	29-32	36-39	43-46	1-22	2-23	3-24	4-25	5-26	6-27	7-28
1-5	8-12	15-19	22-26	29-33	36-40	43-47	1-29	2-30	3-31	4-32	5-33	6-34	7-35
1-6	8-13	15-20	22-27	29-34	36-41	43-48	1-36	2-37	3-38	4-39	5-40	6-41	7-42
1-7	8-14	15-21	22-28	29-35	36-42	43-49	1-43	2-44	3-45	4-46	5-47	6-48	7-49
2-3	9-10	16-17	23-24	30-31	37-38	44-45	8-15	9-16	10-17	11-18	12-19	13-20	14-21
2-4	9-11	16-18	23-25	30-32	37-39	44-46	8-22	9-23	10-24	11-25	12-26	13-27	14-28
2-5	9-12	16-19	23-26	30-33	37-40	44-47	8-29	9-30	10-31	11-32	12-33	13-34	14-35
2-6	9-13	16-20	23-27	30-34	37-41	44-48	8-36	9-37	10-38	11-39	12-40	13-41	14-42
2-7	9-14	16-21	23-28	30-35	37-42	44-49	8-43	9-44	10-45	11-46	12-47	13-48	14-49
3-4	10-11	17-18	24-25	31-32	38-39	45-46	15-22	16-23	17-24	18-25	19-26	20-27	21-28
3-5	10-12	17-19	24-26	31-33	38-40	45-47	15-29	16-30	17-31	18-32	19-33	20-34	21-35
3-6	10-13	17-20	24-27	31-34	38-41	45-48	15-36	16-37	17-38	18-39	19-40	20-41	21-42
3-7	10-14	17-21	24-28	31-35	38-42	45-49	15-43	16-44	17-45	18-46	19-47	20-48	21-49
4-5	11-12	18-19	25-26	32-33	39-40	46-47	22-29	23-30	24-31	25-32	26-33	27-34	28-35
4-6	11-13	18-20	25-27	32-34	39-41	46-48	22-36	23-37	24-38	25-39	26-40	27-41	28-42
4-7	11-14	18-21	25-28	32-35	39-42	46-49	22-43	23-44	24-45	25-46	26-47	27-48	28-49
5-6	12-13	19-20	26-27	33-34	40-41	47-48	29-36	30-37	31-38	32-39	33-40	34-41	35-42
5-7	12-14	19-21	26-28	33-35	40-42	47-49	29-43	30-44	31-45	32-46	33-47	34-48	35-49
6-7	13-14	20-21	27-28	34-35	41-42	48-49	36-43	37-44	38-45	39-46	40-47	41-48	42-49

Appendix B

Overwiev of errors caused by misalignments

In this attachment result of simulations are summarized in Tables showing the maximal errors for each distance group (X1 ... X7, Y1 ... Y7, D1, D2, form errors and absolute value of diameter errors) and corresponding misalignment. in used distance group for every value of misalignment. To make results easier to understand, tables will be color coded. Cells with limit value (according to Table 6.2) will be colored green and maximum value in distances errors, errors of form or diameter errors will be colored green. Other values will be colored in smooth color range between these two extremes as is shown in Table B.1.

Table B.1: Colors legend for tables with results

Limit value	Max. value of the group

Table B.2: Maximal errors of all distance groups, form and diameter fol detector tilt $\Delta\vartheta$.

ϑ	0.01 °	0.02 °	0.03 °	0.05 °	0.1 °	0.2 °	0.3 °	0.4 °	0.5 °	1 °	1.5 °
X1 [µm]	0.9	1.0	1.8	3.3	6.5	13.1	19.9	26.8	33.3	66.9	99.8
X2 [µm]	0.5	1.3	1.6	2.1	4.4	8.6	13.4	17.9	22.3	44.7	66.7
X3 [µm]	0.6	0.6	0.5	1.2	1.8	4.2	6.5	8.5	10.5	21.9	33.0
X4 [µm]	0.3	0.6	0.4	0.4	0.7	0.5	0.7	0.2	0.2	0.5	0.7
X5 [µm]	0.3	1.0	0.9	1.0	2.3	4.0	6.5	8.7	10.6	22.2	33.1
X6 [µm]	0.7	0.9	1.2	2.1	4.3	8.9	13.3	17.5	22.2	44.5	66.7
X7 [µm]	1.1	1.2	2.0	3.2	6.3	13.5	19.8	26.6	33.8	66.6	100.3
MAX X [µm]	1.1	1.3	2.0	3.3	6.5	13.5	19.9	26.8	33.8	66.9	100.3
Y1 [µm]	0.3	0.7	1.3	1.7	3.2	6.8	10.2	13.9	17.2	35.5	55.1
Y2 [µm]	0.5	0.6	1.1	1.6	3.3	6.5	10.2	13.5	17.3	35.6	55.4
Y3 [µm]	0.3	1.0	1.5	2.0	3.2	6.4	10.0	13.5	17.2	35.9	55.0
Y4 [µm]	0.8	0.9	1.1	1.6	3.3	6.7	10.2	13.7	17.9	36.2	55.7
Y5 [µm]	0.9	1.1	1.0	1.8	3.4	6.7	10.2	13.8	17.6	36.0	55.6
Y6 [µm]	0.8	0.9	1.3	2.1	3.5	6.8	10.5	14.0	17.5	36.1	55.7
Y7 [µm]	0.5	1.0	1.2	1.5	3.3	6.8	10.0	14.2	17.7	36.0	55.6
MAX Y [µm]	0.9	1.1	1.5	2.1	3.5	6.8	10.5	14.2	17.9	36.2	55.7
Form [µm]	16.8	15.6	16.4	16.6	15.7	17.4	18.6	18.7	17.1	18.1	19.3
Diameter [µm]	0.8	0.6	1.0	1.2	1.0	1.6	1.6	1.8	2.2	4.2	5.6

Table B.3: Maximal errors of all distance groups, form and diameter fol detector slant φ

φ	0.1 °	0.2 °	0.3 °	0.4 °	0.5 °	0.6 °	0.75 °	1 °	1.5 °
X1 [µm]	0.3	0.4	0.5	1.0	1.0	1.2	3.1	5.2	10.9
X2 [µm]	0.7	0.4	0.4	0.6	1.0	1.3	2.3	4.4	12.0
X3 [µm]	1.1	0.7	1.1	1.0	1.1	2.3	3.4	4.7	12.8
X4 [µm]	0.3	0.7	0.4	1.1	0.9	1.8	2.4	4.6	13.3
X5 [µm]	0.5	0.5	0.7	0.8	1.0	1.8	2.6	4.2	12.2
X6 [µm]	0.4	0.4	0.7	0.6	0.9	1.4	2.9	4.1	11.5
X7 [µm]	0.5	0.7	0.3	0.7	1.1	1.3	2.3	4.8	12.0
MAX X [µm]	1.1	0.7	1.1	1.1	1.1	2.3	3.4	5.2	13.3
Y1 [µm]	0.5	0.3	0.3	0.4	0.2	0.1	0.4	1.4	2.5
Y2 [µm]	0.3	0.1	0.6	0.4	0.3	0.2	0.6	0.6	0.5
Y3 [µm]	0.6	0.4	0.5	0.7	0.4	0.5	0.5	0.5	0.5
Y4 [µm]	0.5	0.9	1.1	0.6	0.5	0.7	0.8	0.8	1.1
Y5 [µm]	0.4	0.4	0.6	0.2	0.2	0.3	0.5	0.3	0.5
Y6 [µm]	0.5	0.6	0.5	0.5	0.5	0.6	0.5	0.5	0.8
Y7 [µm]	0.3	0.5	0.4	0.5	0.6	0.3	0.6	0.7	0.8
MAX Y [µm]	0.6	0.9	1.1	0.7	0.6	0.7	0.8	1.4	2.5
Form [µm]	16.6	16.1	16.7	18.0	19.0	21.8	25.4	47.9	63.3
Diameter [µm]	0.8	0.6	0.8	1.0	0.8	1.0	2.2	3.8	11.6

Table B.4: Maximal errors of all distance groups, form and diameter for detector skew $\Delta\eta$, with determination of rotation axis position only in middle slice.

$\Delta\eta$	0.05 °	0.075 °	0.1 °	0.2 °	0.3 °	0.4 °
X1 [µm]	0.5	0.5	1.1	9.7	50.1	16.7
X2 [µm]	0.4	0.5	0.7	3.4	48.9	12.6
X3 [µm]	0.6	0.5	0.7	1.3	4.4	10.6
X4 [µm]	0.5	0.6	0.6	0.7	0.8	3.1
X5 [µm]	0.6	0.5	0.8	1.8	4.3	9.6
X6 [µm]	0.4	0.5	0.7	1.3	10.9	14.7
X7 [µm]	0.6	0.6	0.8	15.6	13.4	26.5
MAX X [µm]	0.6	0.6	1.1	15.6	50.1	26.5
Y1 [µm]	0.4	0.5	0.9	9.8	52.8	8.4
Y2 [µm]	0.6	0.7	0.5	4.8	37.4	6.4
Y3 [µm]	0.8	0.6	0.5	1.1	13.8	2.6
Y4 [µm]	0.9	0.8	0.8	0.6	0.8	1.5
Y5 [µm]	0.5	0.3	0.6	0.5	12.5	8.9
Y6 [µm]	0.3	0.6	0.6	3.9	13.5	10.0
Y7 [µm]	0.4	0.6	0.8	1.6	22.4	11.4
MAX Y [µm]	0.9	0.8	0.9	9.8	52.8	11.4
Form [µm]	19.0	24.3	35.0	75.7	76.1	76.4
Diameter [µm]	1.4	2.0	3.0	40.0	98.8	130.2

Table B.5: Results of rotation axis shift in x direction, maximum values of errors. No software compensation of misalignment was used.

Δx_r [mm]	0.02	0.03	0.04	0.05	0.1
X1 [µm]	0.8	1.1	2.5	6.1	10.5
X2 [µm]	0.7	1.0	1.6	3.0	14.9
X3 [µm]	0.9	0.9	1.5	5.3	11.0
X4 [µm]	0.6	1.0	1.5	4.9	20.5
X5 [µm]	1.1	1.1	1.8	3.9	22.5
X6 [µm]	0.9	1.0	1.4	2.7	7.1
X7 [µm]	0.5	1.6	1.4	4.9	5.8
MAX X [µm]	1.1	1.6	2.5	6.1	22.5
Y1 [µm]	0.5	0.5	0.8	2.6	3.4
Y2 [µm]	0.3	0.4	1.2	2.4	1.3
Y3 [µm]	0.6	0.7	0.9	2.1	1.7
Y4 [µm]	1.2	0.5	0.7	1.4	3.6
Y5 [µm]	0.5	0.8	0.7	1.6	2.4
Y6 [µm]	0.6	0.7	0.8	1.3	2.0
Y7 [µm]	0.7	0.6	1.0	1.3	3.3
MAX Y [µm]	1.2	0.8	1.2	2.6	3.6
Form [µm]	20.6	30.7	54.4	69.6	68.9
Diameter [µm]	2.2	4.8	10.6	26.8	63.2

Table B.6: Maximal errors of all distance groups, form and diameter for rotation axis tilt ϑ_r.

ϑ_r	0.01 °	0.02 °	0.05 °	0.1 °	0.2 °	0.3 °	0.4 °	0.5 °	1 °	1.5 °
X1 [µm]	0.5	1.1	1.5	2.8	5.9	10.6	19.2	26.9	57.7	62.0
X2 [µm]	0.6	0.6	1.1	1.8	4.0	7.1	12.8	17.1	41.2	42.6
X3 [µm]	0.7	0.8	0.7	1.7	2.7	3.8	6.2	9.4	20.2	26.6
X4 [µm]	0.6	0.7	0.6	0.4	0.5	0.6	0.6	0.6	1.9	4.6
X5 [µm]	0.7	0.9	0.7	1.2	2.3	3.4	6.9	9.4	20.3	34.5
X6 [µm]	0.6	0.8	1.1	2.2	4.2	7.0	13.9	18.9	39.5	50.2
X7 [µm]	0.5	1.1	1.7	2.9	5.9	10.4	20.2	26.9	56.4	64.7
MAX X [µm]	0.7	1.1	1.7	2.9	5.9	10.6	20.2	26.9	57.7	64.7
Y1 [µm]	0.8	0.9	2.0	3.6	7.6	10.1	12.3	17.2	22.1	45.8
Y2 [µm]	0.6	0.7	2.0	3.7	6.7	11.1	13.8	16.9	31.3	35.8
Y3 [µm]	0.7	0.9	2.2	3.8	7.4	10.5	13.9	17.8	32.0	42.4
Y4 [µm]	0.9	1.2	2.1	3.4	6.7	10.2	13.9	17.3	35.6	55.2
Y5 [µm]	0.6	0.7	1.6	3.5	7.0	10.6	14.2	16.7	35.6	44.5
Y6 [µm]	0.4	0.7	1.6	3.2	6.6	10.7	13.0	18.0	27.5	41.1
Y7 [µm]	0.7	0.9	1.7	3.4	6.9	10.4	15.3	16.4	26.3	33.7
MAX Y [µm]	0.9	1.2	2.2	3.8	7.6	11.1	15.3	18.0	35.6	55.2
Form [µm]	16.3	15.2	17.9	28.0	57.1	61.8	77.0	74.8	75.4	77.3
Diameter [µm]	0.8	0.8	1.0	1.0	2.0	2.6	12.0	8.6	24.6	60.4

Table B.7: Maximal errors of all distance groups, form and diameter for rotation axis skew η_r.

η_r	0.05	0.075	0.1	0.2	0.3	0.4
X1 [µm]	0.6	0.5	0.8	35.7	46.9	56.0
X2 [µm]	0.3	0.5	0.6	5.3	38.2	49.1
X3 [µm]	0.8	0.7	0.9	0.8	8.2	26.1
X4 [µm]	0.7	0.8	0.3	0.4	0.9	3.0
X5 [µm]	0.5	0.6	0.5	0.8	7.7	5.7
X6 [µm]	0.5	0.6	0.9	1.6	24.2	16.2
X7 [µm]	0.3	0.6	1.0	8.4	32.6	45.3
MAX X [µm]	0.8	0.8	1.0	35.7	46.9	56.0
Y1 [µm]	0.5	0.4	0.5	23.7	49.5	59.3
Y2 [µm]	0.5	0.3	0.5	10.6	30.6	35.8
Y3 [µm]	0.7	0.5	0.5	1.9	9.0	24.6
Y4 [µm]	0.6	0.5	0.8	1.7	2.5	2.6
Y5 [µm]	0.5	0.4	0.4	1.3	4.9	24.7
Y6 [µm]	0.6	0.6	0.7	2.2	24.7	51.1
Y7 [µm]	0.3	0.6	0.8	4.7	29.0	57.2
MAX Y [µm]	0.7	0.6	0.8	23.7	49.5	59.3
Form [µm]	18.4	22.7	35.4	74.0	79.4	79.7
Diameter [µm]	1.2	1.8	3.4	37.6	92.4	118.8

Appendix C

Documents

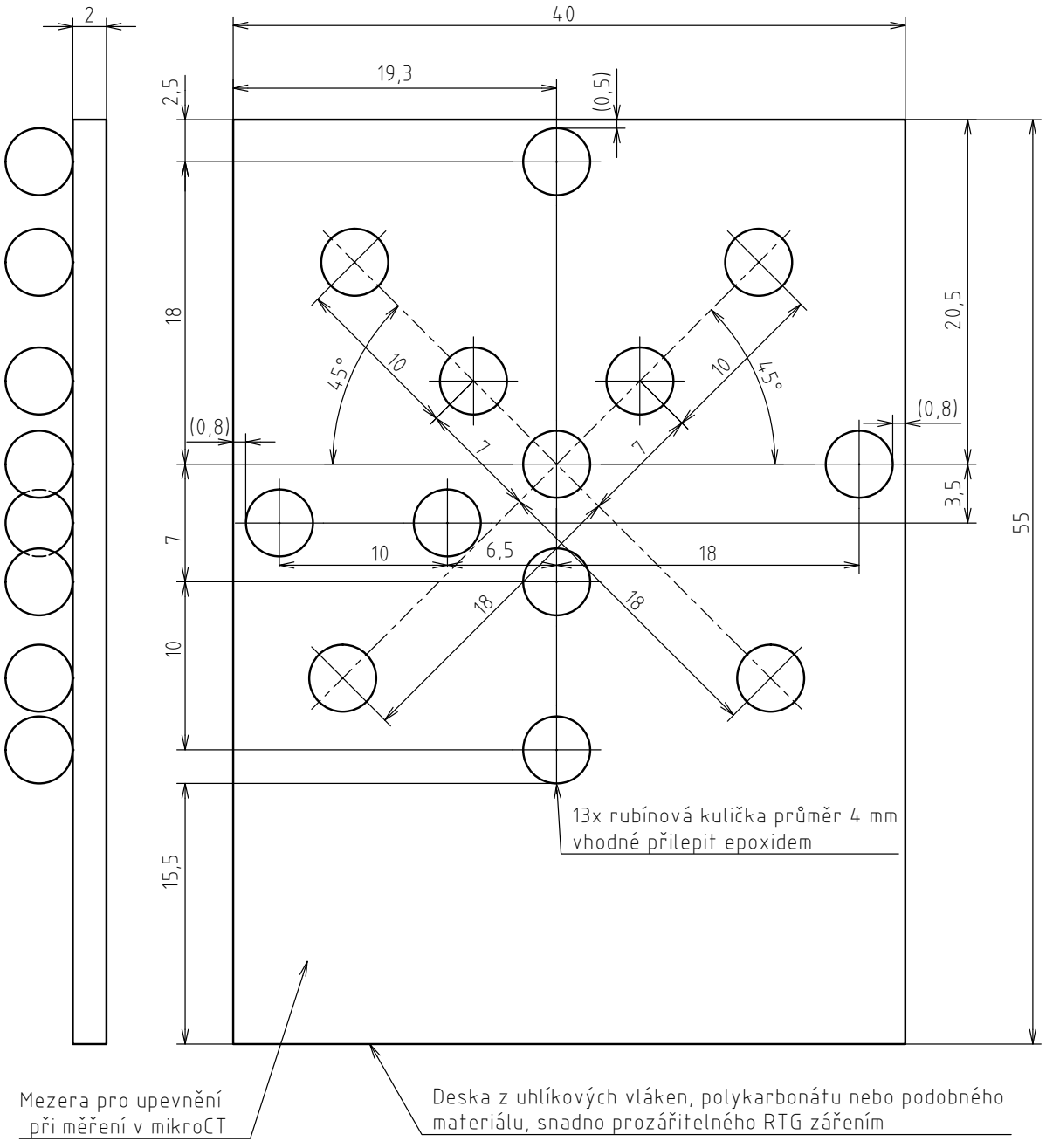

Po konzultaci lze upravit parametry aby vyhovali požadavkům pro výrobu a měření na dotykovém CMM (tloušťka desky, průměr a vzdálenosti kuliček)

	Struktura povrchu/Gen. rough.:		Hrany/ Edges: ⌊-0,1 ⌊+0,3	
Materiál	Kreslil/ Drawn: Blažek	1/25/2019	Přesnost/ Gen. tolerances: ISO 2768-mK	
Hm./Weight: N/A	Uvolnil/ Released:		Tolerování dle/ Tolerance to: ISO 8015	
Měř./ Scale: 4 : 1	Název/Title: Fantom1 – měření chyb délky		Projekt/Project:	
			Číslo položky/Part number:	Rev.
	Jednotka/Unit: mm		Format: A3	List/Sheet: 1 z/of 1

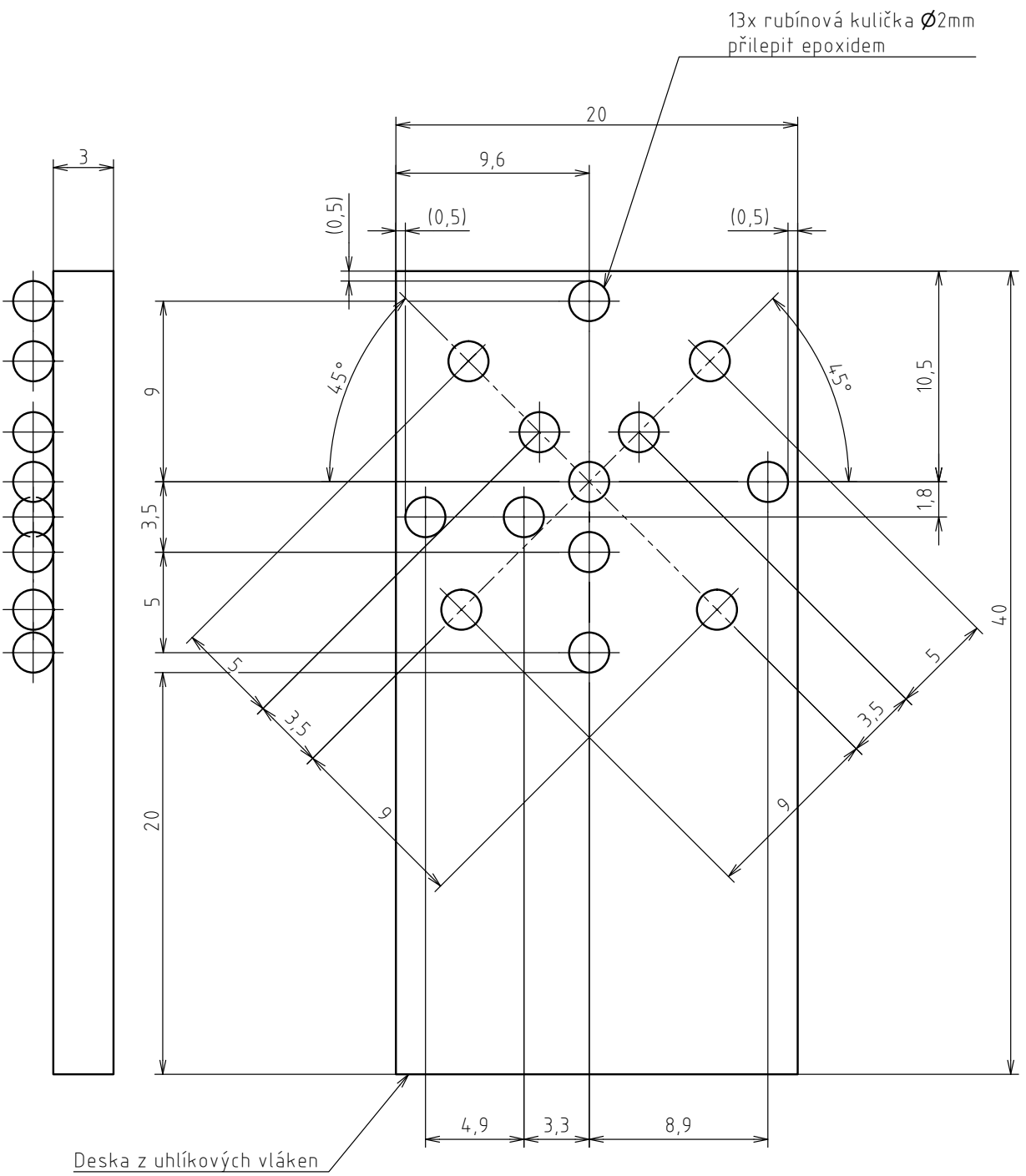

Po konzultaci lze upravit parametry aby vyhovali požadavkům pro výrobu a měření na dotykovém CMM (tloušťka desky, průměr a vzdálenosti kuliček)

	Struktura povrchu/Gen. rough.:		Hrany/ Edges: ⌴-0,1 ⌵+0,3	
Materiál	Kreslil/ Drawn: Blažek	1/25/2019	Přesnost/ Gen. tolerances: ISO 2768-mK	
Hm./Weight: N/A	Uvolnil/ Released:		Tolerování dle/ Tolerance to: ISO 8015	
Měř./ Scale: 5 : 1	Název/Title: Ball plate 20mm		Projekt/Project:	
			Číslo položky/Part number:	Rev.
	Jednotka/Unit: mm		Format: A3	List/Sheet: 1 z/of 1

Český metrologický institut
Okružní 31, 638 00 Brno
tel. +420 545 555 111
www.cmi.cz

Pracoviště: Oblastní inspektorát Brno, Okružní 31, 638 00 Brno
Oddělení primární nanometrologie a technické délky, tel. +420 545 555 111, fax +420 545 555 183

KALIBRAČNÍ LIST

6014-KL-D0100-19

Datum vystavení : 7. březen 2019

Zákazník	:	CEITEC BUT Purkyňova 123, 612 00 Brno
Měřidlo	:	ballplate
Výrobce	:	ČMI
Identifikační číslo	:	č. 1
Rozsah	:	-
Použité etalony	:	Souřadnicový měřicí stroj EXEL 4520, MicroVu, ev.č. EC45201016 Kalibrační list 6014-KL-F0022-17
Kalibrační postup	:	Optické snímání
Podmínky měření	:	Teplota vzduchu (20,0 ± 0,5) °C
Nejistota měření	:	U = 0,0010 mm

Standardní nejistota měření byla určena v souladu s dokumentem EA 4/02. Uvedená rozšířená nejistota měření je součinem standardní nejistoty měření a koeficientu rozšíření k, který odpovídá pokrytí asi 95 %, což pro normální rozdělení odpovídá koeficientu k = 2.

Výsledky kalibrace byly získány za podmínek a s použitím postupu uvedených v tomto kalibračním listě a vztahují se pouze k době a místu provedení kalibrace.

Datum kalibrace : 7. březen 2019

Kalibraci provedl:

Ing. Václav Duchoň

Český metrologický institut -60-

Vedoucí oddělení:

Mgr. Petr Klapetek, Ph.D.

Výsledky kalibrace:

	X [mm]	Y [mm]
S1	0,0000	0,0000
S2	9,9935	-0,0189
S3	16,9976	-0,0250
S4	35,0407	0,0020
S5	13,5564	16,5586
S6	4,3189	12,8188
S7	29,1323	12,1120
S8	13,5606	6,4880
S9	21,9530	4,9313
S10	22,0172	-4,9958
S11	4,2290	-12,7615
S12	17,0547	-18,0306
S13	29,1232	-12,0524

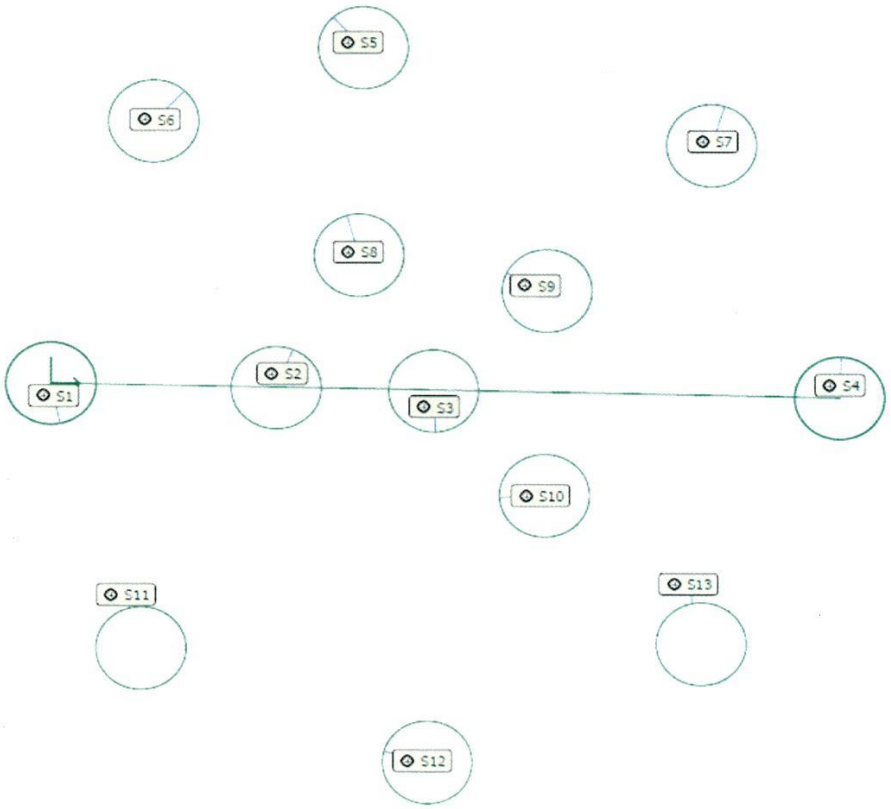

Český metrologický institut
Oblastní inspektorát Brno
Okružní 31
638 00 Brno
-3-

Konec kalibračního listu